EVOLUTION OF MAGNETOHYDRODYNAMIC WAVES IN LOW LAYERS OF A CORONAL HOLE

FRANCESCO PUCCI[1], MARCO ONOFRI[2], AND FRANCESCO MALARA[1]
[1] Dipartimento di Fisica, Università della Calabria, Rende (CS), I-87036, Italy
[2] Tri Alpha Energy, PO Box 7010, Rancho Santa Margarita, CA 92688, USA

ABSTRACT

Although a coronal hole is permeated by a magnetic field with a dominant polarity, magnetograms reveal a more complex magnetic structure in the lowest layers, where several regions of opposite polarity of typical size of the order of 10^4 km are present. This can give rise to magnetic separatrices and neutral lines. MHD fluctuations generated at the base of the coronal hole by motions of the inner layer of the solar atmosphere may interact with such inhomogeneities, leading to the formation of small scales. This phenomenon is studied on a 2D model of a magnetic structure with an X-point, using 2D MHD numerical simulations. This model implements a method of characteristics for boundary conditions in the direction outer-pointing to Sun surface to simulate both wave injection and exit without reflection. Both Alfvénic and magnetosonic perturbations are considered, and they show very different phenomenology. In the former case, an anisotropic power-law spectrum forms with a dominance of perpendicular wavevectors at altitudes $\sim 10^4$ km. Density fluctuations are generated near the X-point by Alfvén wave magnetic pressure and propagate along open fieldlines at a speed comparable to the local Alfvén velocity. An analysis of energy dissipation and heating caused by the formation of small scales for the Alfvénic case is presented. In the magnetosonic case, small scales form only around the X-point, where a phenomenon of oscillating magnetic reconnection is observed to be induced by the periodic deformation of the magnetic structure due to incoming waves.

Key words: magnetic reconnection – Sun: corona – waves

Online-only material: color figure

1. INTRODUCTION

Low-frequency fluctuations in the domain of magnetohydro-dynamics (MHD) are believed to populate the plasma of the solar corona. These fluctuations originate from photospheric motions and propagate up to the corona along the magnetic field that permeates the solar atmosphere. In situ measurements have revealed MHD fluctuations in the solar wind for several decades (Belcher & Davis 1971); this is considered to be an indirect indication of the presence of the same kind of fluctuations in the corona, from where the solar wind emanates. Evidence of velocity fluctuations of the order $\delta v \sim 30$–$50 \, \mathrm{km \, s^{-1}}$ in the corona at unresolved spatial and temporal scales has been deduced from nonthermal broadening of coronal lines (Acton et al. 1981; Warren et al. 1997; Chae et al. 1998). In recent years, velocity fluctuations have also been ubiquitously detected in the corona (Tomczyk et al. 2007; Tomczyk & McIntosh 2009). Such fluctuations appear to propagate along magnetic lines at a speed that is consisted with estimations of the Alfvén velocity; thus they are considered to be Alfvén waves, although a different interpretation has also been proposed in terms of kink magnetoacoustic waves (Van Doorsselaere et al. 2008). More recently, Alfvén waves with energy sufficient to power the quiet corona and fast solar wind have been found (McIntosh et al. 2011). Moreover, indirect evidences of Alfvén waves in coronal holes have also been reported (see Banerjee et al. 2011 for a review).

Waves and turbulence are considered to be one of the energy sources responsible for solar wind expansion (Sorriso-Valvo et al. 2007; Marino et al. 2011; Hellinger et al. 2013). For instance, observed variations of proton temperature with the heliocentric distance are inconsistent with a simple adiabatic expansion, which instead requires a continuous heat deposition along the solar wind path (e.g., Matthaeus et al. 1999a).

Turbulence represents the best candidate to explain such an extended heating. Moreover, turbulence formation has been proposed as a mechanism responsible for solar wind acceleration in the near-Sun region. The main idea is that waves produced by photospheric motions propagate upward in coronal open-field regions, which is where the solar wind originates. As a result of vertical stratification and magnetic field expansion, these waves are partially reflected downward. Nonlinear interactions between MHD waves propagating in two opposite directions generate an energy cascade toward small scales, eventually dissipating part of the wave energy, which would then be responsible for both coronal heating and wind acceleration (Matthaeus et al. 1999b). Several models have been proposed within such a framework: a model of Alfvén wave propagation in the chromosphere and the corona, in which heating and acceleration are a consequence of compressive waves and shocks formation (Suzuki & Inutsuka 2005); a model ranging from the chromosphere to the corona, which includes the effects of pressure and acoustic wave gradients (Cranmer et al. 2007); models where nonlinear effects are modeled by phenomenological terms (Verdini & Velli 2007), by a simplified representation of the wavevector space (shell model; Verdini et al. 2009), or a strong turbulence closure (Verdini et al. 2010).

In these models, the background structure where perturbations propagate contains a unipolar magnetic field possibly varying on a relatively large spatial scale, at least in the coronal part of the considered domain. Indeed, coronal holes and solar wind are both characterized by a mainly unipolar magnetic field (McComas et al. 2000). However, magnetograms taken in coronal hole regions show a complex structure at low altitudes that is characterized by areas of both magnetic polarities (Zhang et al. 2006). Thus, the magnetic field at low altitude in a coronal hole has a complex 3D structure containing open fieldlines

extending to larger altitudes and closed fieldlines connecting regions of opposite polarities (Ito et al. 2010). Perturbations generated by photospheric motions, which cross this complex structure when propagating upward, couple with gradients of the background. As a result, small scales are generated in the perturbations. The present paper focuses on the mechanism of small-scale formation due to the coupling between perturbation and background inhomogeneity, which has not been considered in the previously cited models.

The evolution of hydromagnetic perturbations propagating in an inhomogeneous background has been widely studied. In a 2D inhomogeneous background, where the Alfvén velocity varies in directions perpendicular to the magnetic field, two mechanisms have been investigated in detail: (1) phase-mixing (Heyvaerts & Priest 1983), in which differences in group velocity at different locations progressively bend wavefronts; and (2) resonant absorption that concentrates the wave energy in a narrow layer where the local wave frequency matches a characteristic frequency (Alfvén or cusp). These processes have been studied by investigating normal modes of the inhomogeneous structure (Kappraff et al. 1977; Mok & Einaudi 1985; Steinolfson 1985; Davila 1987; Hollweg 1987; Califano et al. 1990, 1992) and by considering the evolution of an initial disturbance (Lee & Roberts 1986; Malara et al. 1992, 1996). The effects of density stratification and magnetic line divergence (Ruderman 1998), as well as nonlinear coupling with compressive modes Nakariakov et al. (1997, 1998), have also been considered. The propagation of MHD waves in magnetic fields containing null points has been studied in detail too (Landi et al. 2005) (see also McLaughlin et al. 2010 for a review).

Studying the evolution of MHD perturbations in 3D structures is more complex. In particular, the evolution of Alfvén waves has been studied using a simplified approach based on a Wentzel–Keller–Brillouin (WKB) method first proposed by Similon & Sudan (1989), and was also studied in detail both from a general point of view (Petkaki et al. 1998; Malara et al. 2000, 2003) and in the context of the coronal heating problem (Malara et al. 2005, 2007). The same method was used by Malara et al. (2012), and in more detail by Malara (2013), to study the evolution of Alfvén waves propagating in a 3D magnetic field that models the magnetic structure in an open fieldline region with the previously described features (Ito et al. 2010). The results showed that small scales form in the Alfvénic perturbation at very low altitudes ($\sim 10^5$ km above the coronal base) as a consequence of its interactions with specified equilibrium field inhomogeneities. Such small scales are located at magnetic separatrices and the resulting spectra of the perturbation have a power-law dependence, with a large prevalence of wave vectors perpendicular to the magnetic field.

The main limitations in the model by Malara (2013) are due to the WKB approximation, which assumes that the perturbation wavelength λ is much smaller than the scale of variation of the equilibrium structure, which is of the order of $L_{\rm eq} \sim 3 \times 10^4$ km. Assuming a typical Alfvén velocity $c_A \sim 500\,{\rm km\,s^{-1}}$ and a timescale of perturbations $\tau \sim 500$ s, the wavelength in the direction parallel to the magnetic field is $\lambda_{||} = c_A \tau \sim 2.5 \times 10^5$ km. Thus, the assumption of small wavelength is somewhat questionable. Moreover, all compressive effects have been neglected in this model.

In the present paper, we try to overcome these limitations of the WKB method by using full compressible MHD simulations instead. In particular, a simplified 2D version of the equilibrium magnetic field used in Malara (2013) is considered, in which both Alfvénic and magnetosonic fluctuations are generated by transverse motions at the base of the domain. The dynamics of the system and the generation of small scales in perturbations after crossing the background inhomogeneity are investigated. Most of the results obtained by the WKB approach are recovered, along with new effects, which are mainly related to the compressive component of perturbations. The implications for the problem of solar wind acceleration and understanding the presence of density fluctuations in the open fieldline corona are discussed.

2. THE MODEL

We consider an open-field line region of the solar corona. The configuration is given by an inhomogeneous MHD equilibrium with superimposed fluctuations that propagate in the upward direction. We study the dynamics of the interaction between fluctuations and the inhomogeneous background using numerical simulations.

The spatial domain represents a small portion of a coronal hole that is located just above the coronal base. We indicate all quantities relating to the equilibrium configuration by the upper index "(0)." A detailed description of the equilibrium magnetic field $\mathbf{B}^{(0)}$ is available elsewhere (Malara 2013); in the following, we summarize the assumptions and describe the derivation. Although a coronal hole is characterized by an essentially unipolar magnetic field, magnetograms of coronal hole regions (Zhang et al. 2006; Ito et al. 2010) show that there are low-lying regions where the photospheric magnetic field has a polarity opposite to the dominant one. The areas of the two polarities appear to be intermixed, forming a complex structure with different spatial scales ranging from $\sim 10^9$ cm down to the resolution limit. The area corresponding to the flux with the dominant polarity represents $\sim 70\%$ of the total area, whereas the remaining 30% corresponds to the opposite polarity (Zhang et al. 2006). The coronal magnetic field above such regions should have a complex structure: well-closed magnetic lines connecting the regions of opposite polarity should be present, along with open magnetic lines emanating from dominant polarity regions. At sufficiently high altitudes, only open magnetic lines should be found, with the magnetic field structure becoming less complex (Zhang et al. 2006; Ito et al. 2010). The magnetic field model considered here tries to represent the above described features in a very simplified form.

Due to the smallness of the considered spatial domain, we neglect curvature effects due to the spherical geometry, and use a Cartesian reference frame XYZ in which the YZ plane corresponds the coronal base, while the X axis is directed vertically upward. The spatial domain is $D = \{(X, Y, Z)\} = [0, L] \times [0, R_y L] \times [0, R_z L]$, where L is of the order of the characteristic scale of the magnetic field at the coronal base, while the aspect ratios R_y and R_z are quantities of order 1. The magnetic field structure is more complex at low altitudes, while the influence of boundary conditions at the base $X = 0$ decreases with increasing altitude X. Then, we assume that the equilibrium magnetic field $\mathbf{B}^{(0)}(\mathbf{r})$ becomes uniform and vertically directed at large altitudes X:

$$\lim_{X \to +\infty} \mathbf{B}^{(0)}(X, Y, Z) = B_0 \mathbf{e}_x, \qquad (1)$$

where B_0 is a constant and $\mathbf{e}_x$ is the unit vector in the X direction. Moreover, we choose $B_0 > 0$ corresponding to a positive polarity at sufficiently high altitudes. Periodicity in the

horizontal Y and Z directions is assumed. Because the coronal plasma has a low β, the equilibrium condition requires that $\mathbf{B}^{(0)}$ is a force-free magnetic field:

$$\nabla \times \mathbf{B}^{(0)} = \alpha \mathbf{B}^{(0)}, \qquad (2)$$

where the scalar quantity α is constant along fieldlines. The condition (1) implies that α is vanishing at large altitudes and along open fieldlines. Thus, the simplest choice is to assume that $\alpha = 0$ in the whole domain. This assumption is expressed by the condition

$$\mathbf{B}^{(0)} = -\nabla \Phi, \qquad (3)$$

where the scalar potential Φ must satisfy the Laplace equation

$$\nabla^2 \Phi = 0, \qquad (4)$$

which follows from the divergence-free condition for $\mathbf{B}^{(0)}$. Using periodicity, Φ can be expanded in a Fourier series along Y and Z,

$$\Phi(X, Y, Z) = \sum_{k_y, k_z} \hat{\Phi}_{k_y, k_z}(X) \, e^{i(k_y Y + k_z Z)}, \qquad (5)$$

where $k_y = 2\pi n/(R_y L)$ and $k_z = 2\pi m/(R_z L)$, with n and m integers. Laplace Equation (4) gives an equation for the Fourier coefficients $\hat{\Phi}_{k_y, k_z}(X)$:

$$\frac{d^2 \hat{\Phi}_{k_y, k_z}(X)}{dX^2} = -\left(k_y^2 + k_z^2\right) \hat{\Phi}_{k_y, k_z}(X). \qquad (6)$$

The solution of Equation (6) for $k_y = k_z = 0$ is

$$\hat{\Phi}_{0,0}(X) = a + bX \qquad (7)$$

with a and b constants corresponding to a homogeneous magnetic field. We can set $a = 0$ without lack of generality, while we choose $b = -B_0$. The latter condition is related to the assumption (1). The solution for $(k_y, k_z) \neq (0, 0)$ is

$$\hat{\Phi}_{k_y, k_z}(X) = A_{k_y, k_z} e^{-h(k_y, k_z)X} + C_{k_y, k_z} e^{h(k_y, k_z)X} \qquad (8)$$

with

$$h(k_y, k_z) = \sqrt{k_y^2 + k_z^2} \qquad (9)$$

and A_{k_y, k_z} and C_{k_y, k_z} constants. The term proportional to C_{k_y, k_z} would give a magnetic field that diverges in the limit $X \to +\infty$. For this reason we discard this solution and choose $C_{k_y, k_z} = 0$. Then, using expressions (7) and (8), we get:

$$\Phi(X, Y, Z) = \sum_{k_y, k_z \neq (0,0)} A_{k_y, k_z} e^{-h(k_y, k_z)X + i(k_y Y + k_z Z)} - B_0 X. \qquad (10)$$

The last equation can be simplified because Φ is a real quantity, which implies that $A_{-k_y, -k_z} = A_{k_y, k_z}^*$, where the asterisk indicates complex conjugate. Using this condition, expression (10) can be written in the following form containing only real quantities:

$$\Phi(X, Y, X) = \sum_{\substack{(k_y, k_z) \neq (0,0) \\ k_z \geqslant 0}} \phi_{k_y, k_z} \cos(k_y Y + k_z Z + \gamma_{k_y, k_z}) e^{-h(k_y, k_z)X} - B_0 X, \qquad (11)$$

where $\phi_{k_y, k_z} = 2\Re(A_{k_y, k_z})$ and the phases γ_{k_y, k_z} can be chosen in the interval $[0, 2\pi]$. Finally, using expression (11) for the

potential from Equation (3), we can calculate the components of the equilibrium magnetic field:

$$B_x^{(0)}(X, Y, Z) = \sum_{\substack{(k_y, k_z) \neq (0,0) \\ k_z \geqslant 0}} h(k_y, k_z) \, \phi_{k_y, k_z} \cos(k_y Y + k_z Z + \gamma_{k_y, k_z})$$
$$\times \, e^{-h(k_y, k_z)X} + B_0 \qquad (12)$$

$$B_y^{(0)}(X, Y, Z) = \sum_{\substack{(k_y, k_z) \neq (0,0) \\ k_z \geqslant 0}} k_y \phi_{k_y, k_z} \sin(k_y Y + k_z Z + \gamma_{k_y, k_z}) e^{-h(k_y, k_z)X} \qquad (13)$$

$$B_z^{(0)}(X, Y, Z) = \sum_{\substack{(k_y, k_z) \neq (0,0) \\ k_z \geqslant 0}} k_z \phi_{k_y, k_z} \sin(k_y Y + k_z Z + \gamma_{k_y, k_z}) e^{-h(k_y, k_z)X}. \qquad (14)$$

Note that the above expressions satisfy condition (1). The equilibrium magnetic field (12)–(14), which is equivalent to the form used by Malara (2013), is a superposition of different harmonics at a given spatial scale determined by the wavevector (k_y, k_z). When many harmonics are present, the resulting magnetic field has a complex structure containing both open and closed fieldlines, with the latter connecting regions of opposite polarity at the base $X = 0$. Magnetic null points and separatrices are also present (Malara 2013). The details of the magnetic structure are determined by the choice of parameters $(B_0, \phi_{k_y, k_z},$ and $\gamma_{k_y, k_z})$. In the present case, the dynamics of the system are studied numerically for a 2D configuration in which all quantities depend only on X and Z. In order to better exploit the finite resolution allowed by the spatial grid, we use a form for $\mathbf{B}^{(0)}$ that is as simple as possible, where only one single term is retained in the sums contained in Equations (12)–(14). This term corresponds to the smallest wave vector $(k_y, k_z) = (0, k_{1z})$, with $k_{1z} = 2\pi/(R_z L)$:

$$B_x^{(0)}(X, Z) = B_0[1 + b_1 \cos(k_{1z} Z) e^{-k_{1z} X}] \qquad (15)$$

$$B_y^{(0)} = 0 \qquad (16)$$

$$B_z^{(0)}(X, Z) = B_0 b_1 \sin(k_{1z} Z) e^{-k_{1z} X}, \qquad (17)$$

where $b_1 = k_{1z} \phi_{0, k_{1z}}/B_0$ and it has been chosen that $\gamma_{0, k_{1z}} = 0$. The above expressions contain two dimensionless quantities: the relative amplitude b_1 of the inhomogeneous component and the aspect ratio R_z. They are determined by requiring the fulfilment of two conditions. (1) The vertical component $B_x^{(0)}$ must change sign along the base $X = 0$ of the spatial domain, which corresponds to the inequality $|b_1| > 1$. In this case there is a magnetic null point above the coronal base ($X > 0$) located at the position $(X_0, Z_0) = (\ln b_1/k_{1z}, \pi/k_{1z})$ for $b_1 > 0$, or $(X_0, Z_0) = (\ln(-b_1)/k_{1z}, 0)$ for $b_1 < 0$. We also require that (2) the null point is inside the considered domain (i.e., $X_0 < L$). Conditions (1) and (2) correspond to

$$1 < |b_1| < e^{2\pi/R_z}. \qquad (18)$$

In particular, we have chosen $b_1 = 2$ and $R_z = \pi$, which satisfy the inequalities (18). In this case the magnetic null point is located at the position $(X_0, Z_0) = (L \ln 2/2, L\pi/2)$. The magnetic field (15)–(17) can be expressed in terms of a vector potential: $\mathbf{B}^{(0)} = \nabla \times (A^{(0)} \mathbf{e}_y)$, where

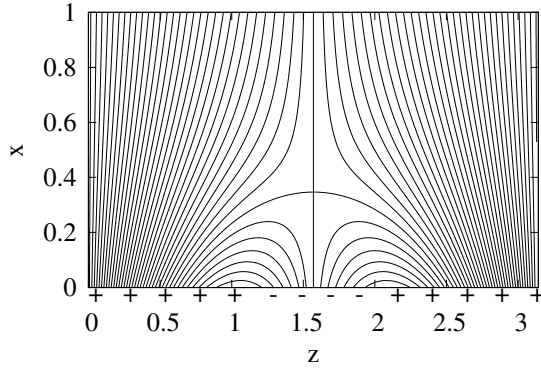$$A^{(0)}(X, Z) = -\frac{B_0 b_1}{k_{1z}} \sin(k_{1z} Z) e^{-k_{1z} X} - B_0 Z. \qquad (19)$$

Figure 1. Magnetic lines of the equilibrium magnetic field $\mathbf{b}^{(0)}$ in the xz plane. The symbols "+" and "−" represent the polarity of the field at $x = 0$.

In Figure 1, magnetic lines of the equilibrium magnetic field $\mathbf{B}^{(0)}$ are represented in the XZ plane. This plot is obtained by drawing the isolines of the vector potential $A^{(0)}$ (Equation (19)). It can be seen that $B_x^{(0)}$ changes sign along the base $X = 0$; it is positive on the left and the right sides and negative in the central part. In the lower part of the domain, both open and closed fieldlines are present, whereas only open fieldlines are found in the upper part of D. An X-type magnetic null point is located at the position (X_0, Z_0). Four separatrices intersect at the X-point: those starting from the base of D separate the two regions of closed and open fieldlines, whereas the separatrix extending above the X-point separates open fieldlines coming from distant parts of the base. Finally, $\mathbf{B}^{(0)}$ tends to become uniform and vertically directed in the uppermost part of D, as required by the condition (1). Thus, despite its simple form, $\mathbf{B}^{(0)}$ reproduces all the features we want to model.

A magnetic field similar to that of our model is typically found at much larger scales in pseudostreamers, which are thin coronal structures extending radially up to several solar radii (Wang et al. 2007). A pair of loop arcades with an X-neutral line in between underlay a pseudostreamer, which is supposed to develop along the vertical separatrix (Wang et al. 2012). Thus the equilibrium magnetic field of our model can be considered a small-scale version of the magnetic structures commonly observed in the corona.

The equilibrium mass density and pressure are assumed to be uniform

$$\rho_m^{(0)}(X, Z) = \rho_{m0} = \text{const}, \quad P^{(0)}(X, Z) = \text{const}, \quad (20)$$

thus neglecting any stratification generated by gravity, whereas the equilibrium velocity is vanishing, $\mathbf{V}^{(0)} = 0$.

MHD waves are superposed on the above described equilibrium. No waves are present at the initial time $\tau = 0$, but they are continuously generated by imposing the velocity at the base $X = 0$. This boundary condition is intended to represent the effects of the motion of underlying denser layers on the coronal plasma, and are specified in the next section.

3. NUMERICAL METHOD

In order to describe the evolution of the model, we numerically solve the nonlinear, compressible, non-ideal, 2D MHD equations

$$\frac{\partial \rho_m}{\partial t} + \nabla \cdot (\rho_m \mathbf{V}) = 0, \quad (21)$$

$$\frac{\partial \mathbf{V}}{\partial t} + (\mathbf{V} \cdot \nabla) \mathbf{V} = -\frac{1}{\rho_m} \nabla P + \frac{1}{4\pi \rho_m} (\nabla \times \mathbf{B}) \times \mathbf{B} + \frac{\tilde{\nu}}{\rho_m} \nabla \cdot \mathbf{\Pi}, \quad (22)$$

$$\frac{\partial \mathbf{B}}{\partial t} = \nabla \times (\mathbf{V} \times \mathbf{B}) + \frac{c^2 \tilde{\eta}}{4\pi} \nabla^2 \mathbf{B}, \quad (23)$$

$$\frac{\partial P}{\partial t} + \nabla \cdot (P\mathbf{V}) + (\gamma - 1) P (\nabla \cdot \mathbf{V}) = \tilde{\kappa} \nabla^2 T + (\gamma - 1)$$
$$\times \left[\frac{c^2 \tilde{\eta}}{(4\pi)^2} (\nabla \times \mathbf{B})^2 + \frac{\tilde{\nu}}{2} \mathbf{\Pi} : \mathbf{\Pi} \right] \quad (24)$$

with

$$T = \frac{\mu m_p}{k_B} \frac{P}{\rho_m} \quad (25)$$

and the components of the tensor $\mathbf{\Pi}$ are

$$\Pi_{ij} = \frac{\partial \mathbf{V}_i}{\partial X_j} + \frac{\partial \mathbf{V}_j}{\partial X_i} - \frac{2}{3} \delta_{ij} \frac{\partial \mathbf{V}_k}{\partial X_k}. \quad (26)$$

In the above equations ρ_m, P, T, $\mathbf{V}$, and $\mathbf{B}$ are the mass density, pressure, temperature, velocity, and magnetic field, respectively. All physical quantities are functions of the spatial variables X and Z and of the time t. $\tilde{\nu}$, $\tilde{\eta}$, and $\tilde{\kappa}$ are the dynamic viscosity, resistivity and, thermal conductivity, respectively, and are assumed constant. k_b is the Boltzmann constant, c is the speed of light, m_p is the proton mass, $\mu \sim 1$ is the mean molecular weight.

We introduce dimensionless quantities

$$x = \frac{X}{L}; \quad z = \frac{Z}{L}; \quad \tau = \frac{c_{A0}}{L} t; \quad \rho = \frac{\rho_m}{\rho_{m0}}; \quad \mathbf{v} = \frac{\mathbf{V}}{c_{A0}};$$
$$\mathbf{b} = \frac{\mathbf{B}}{B_0}; \quad p = \frac{P}{\rho_{m0} c_{A0}^2} \quad (27)$$

In these expressions, $L = 10^9$ cm is the typical size of structures in coronal hole magnetograms (Zhang et al. 2006); $\rho_{m0} = 5 \times 10^{-16}$ g cm^{-3} is a typical density; $c_{A0} = 2.5 \times 10^7$ cm s^{-1} is a typical value of Alfvén velocity in coronal holes (McIntosh et al. 2011); and $B_0 = c_{A0}\sqrt{4\pi \rho_{m0}}$. Using the dimensionless variables, Equations (21)–(24) take the following form:

$$\frac{\partial \rho}{\partial \tau} + \nabla \cdot (\rho \mathbf{v}) = 0, \quad (28)$$

$$\frac{\partial \mathbf{v}}{\partial \tau} + (\mathbf{v} \cdot \nabla) \mathbf{v} = -\frac{1}{\rho} \nabla p + \frac{1}{\rho} (\nabla \times \mathbf{b}) \times \mathbf{b} + \frac{\nu}{\rho} \nabla \cdot \boldsymbol{\sigma}, \quad (29)$$

$$\frac{\partial \mathbf{b}}{\partial \tau} = \nabla \times (\mathbf{v} \times \mathbf{b}) + \eta \nabla^2 \mathbf{b}, \quad (30)$$

$$\frac{\partial p}{\partial \tau} + \nabla \cdot (p\mathbf{v}) + (\gamma - 1) p (\nabla \cdot \mathbf{v})$$
$$= \kappa \nabla^2 \left(\frac{p}{\rho} \right) + (\gamma - 1) \left[\eta (\nabla \times \mathbf{b})^2 + \frac{\nu}{2} \boldsymbol{\sigma} : \boldsymbol{\sigma} \right] \quad (31)$$

with

$$\sigma_{ij} = \frac{\partial \mathbf{v}_i}{\partial x_j} + \frac{\partial \mathbf{v}_j}{\partial x_i} - \frac{2}{3}\delta_{ij}\frac{\partial \mathbf{v}_k}{\partial x_k} \qquad (32)$$

and $\nu = \tilde{\nu}/(L\rho_{m0}c_{A0})$, $\eta = \tilde{\eta}c^2/(4\pi c_{A0}L)$, $\kappa = \tilde{\kappa}\mu m_p/(\kappa_b L\rho_{m0}c_{A0})$.

Using the new variables, the spatial domain D is transformed into the domain $D' = \{(x, z)\} = [0, 1] \times [0, R_z]$. It is worth noting that for the aspect ratio we used, the value $R_z = \pi$, corresponds to the horizontal length $L_z \simeq 3 \times 10^9$ cm. The initial condition is given by the equilibrium structure specified in the previous section. The initial dimensionless density and pressure are $\rho = 1$ and $p = 0.05$, respectively, with the latter corresponding to a plasma beta value:

$$\beta = p\left[\frac{1}{R_z}\int_{D'}\frac{b^2}{2}dxdz\right]^{-1} \approx 5 \times 10^{-2}. \qquad (33)$$

Concerning boundary conditions, the lower boundary $x = 0$ represents the border through which perturbations coming from layers underlying the corona are entering. On this boundary, we impose the value of the velocity field. In particular, we consider two cases.

(a) Uniform oscillatory motion at the base directed in the y direction, $\mathbf{v}(x = 0, z, \tau) = v_1 \sin(\omega\tau)\mathbf{e}_y$, where v_1 and ω are the velocity amplitude and frequency, respectively. This boundary condition generates fluctuations propagating inside the domain with a polarization (y), which is perpendicular both to the equilibrium magnetic field $\mathbf{b}^{(0)}$ and the perturbation wavevector (which is in the xz plane). For this reason we refer to this kind of fluctuation as Alfvénic.

(b) Uniform oscillatory motion at the base directed in the z-direction, $\mathbf{v}(x = 0, z, \tau) = v_1 \sin(\omega\tau)\mathbf{e}_z$. In this case generated fluctuations are polarized in the plane containing both $\mathbf{b}^{(0)}$ and the wavevector. We refer to this kind of fluctuation as magnetosonic.

In both cases, we used the value $\omega = \pi/2$ for the frequency, corresponding to a waveperiod $t_w = 160\,s$, and $v_1 = 0.1$ corresponding to the amplitude $V_1 = 2.5 \times 10^6$ cm s^{-1}, in accordance with observations (McIntosh et al. 2011). The value of other physical quantities at $x = 0$ is calculated using a method of projected characteristics (Nakagawa et al. 1987; Sun et al. 1995; Poinsot & Lele 1993; Grappin et al. 2000; Landi et al. 2005). In our case, we use this method to evaluate ρ, p, and $\mathbf{b}$ in a way that is consistent with the values specified for the velocity field and with the MHD equations. A detailed description of this procedure is given in Appendix A.

The upper boundary $x = 1$ is a free boundary that must allow perturbations propagating inside the domain to exit without reflection. Again, the method of projected characteristics has been implemented on the upper boundary to simulate this physical condition. The details of boundary conditions at $x = 1$ are given in Appendix A. Finally, periodic boundary conditions are imposed in the horizontal z direction.

Equations (28)–(31), with the specified boundary conditions, are numerically solved by employing a Cartesian 2D version of a compressible MHD code that was originally written for 3D cylindrical configurations with time-dependent boundary conditions (Onofri et al. 2007). The uniform spatial grid is formed by $nx \times nz$ points ($nx = 1024, nz = 256$). A sixth-order finite difference method in the x direction and a pseudospectral Fourier method in the z direction are used. Time derivatives are

calculated using a third-order Runge-Kutta scheme. Viscosity, resistivity, and thermal conductivity are uniform over the domain and constant: $\nu = \eta = \kappa = 10^{-3}$.

Equation (31) can be rewritten in the form of an evolution equation for the internal energy density $u = p/(\gamma - 1)$:

$$\frac{\partial u}{\partial \tau} + \nabla \cdot (u\mathbf{v}) + (\gamma - 1)u(\nabla \cdot \mathbf{v}) = \kappa\nabla^2\left(\frac{p}{\rho}\right) + P_\eta + P_\nu, \quad (34)$$

where

$$P_\eta = \eta(\nabla \times \mathbf{b})^2; \qquad P_\nu = \frac{\nu}{2}\boldsymbol{\sigma} : \boldsymbol{\sigma} \qquad (35)$$

are the dissipated power per unit volume due to resistivity and to viscosity, respectively. Other useful quantities are defined by

$$w_\eta(\tau) = \int_{D'}P_\eta(x, z, \tau)\,dxdz; \quad w_\nu(\tau) = \int_{D'}P_\nu(x, z, \tau)\,dxdz, \qquad (36)$$

which represent the dissipated resistive and viscous power integrated over the domain D'. Using Equations (28)–(30) and (34), it is possible to write a conservation law for total energy density in a differential form. Integrating this equation on the domain D' and using the divergence theorem gives the energy conservation equation

$$\frac{dE}{d\tau} + \Phi = 0, \qquad (37)$$

where

$$E = \int_{D'}\left(\frac{1}{2}\rho|\mathbf{v}|^2 + \frac{|\mathbf{b}|^2}{2} + u\right)dxdz \qquad (38)$$

is the total energy per unit length in the domain D', and

$$\Phi = \oint_{\partial D'}\left[\left(\frac{1}{2}\rho|\mathbf{v}|^2 + \gamma u\right)\mathbf{v} + \mathbf{S} + \nu\left((\mathbf{v}\cdot\nabla)\mathbf{v} - (\nabla\cdot\mathbf{v})\mathbf{v}\right)\right.$$
$$\left. -\kappa\nabla\left(\frac{p}{\rho}\right)\right]\cdot\hat{\mathbf{n}}dl. \qquad (39)$$

In this expression, $\mathbf{S} = |\mathbf{b}|^2\mathbf{v} - (\mathbf{v}\cdot\mathbf{b})\mathbf{b} + \eta(\nabla\times\mathbf{b})\times\mathbf{b}$ is the Poynting vector, $\partial D'$ is the contour of D', $\hat{\mathbf{n}}$ is the outer-pointing normal to $\partial D'$, and dl is an infinitesimal piece of $\partial D'$. The quantity (39) represents the energy flux through the boundary that is due to four different effects: advection of matter, Poynting vector flux, viscous forces work along the boundaries, and heat flux. In our particular configuration, the net flux through the boundaries $z = 0$ and $z = R_z = \pi$ is null because of periodicity. Thus, we can write the total flux in the form $\Phi = \Phi_0 + \Phi_1$, where Φ_0 and Φ_1 are the fluxes through the boundaries $x = 0$ and $x = 1$, respectively. Taking into account the form of boundary conditions imposed at these boundaries (see Appendix A), we find

$$\Phi_0 = \int_{x=0}\left[-\eta(\mathbf{b}\cdot\nabla)b_x + \eta\frac{\partial}{\partial x}\left(\frac{|\mathbf{b}|^2}{2}\right) + (\mathbf{v}\cdot\mathbf{b})b_x\right]dz \qquad (40)$$

$$\Phi_1 = \int_{x=1}\left[\left(\frac{1}{2}\rho|\mathbf{v}|^2 + \gamma u\right)v_x + \eta\left((\mathbf{b}\cdot\nabla)b_x - \frac{\partial}{\partial x}\left(\frac{|\mathbf{b}|^2}{2}\right)\right)\right.$$
$$+ |\mathbf{b}|^2 v_x - (\mathbf{v}\cdot\mathbf{b})b_x + \nu$$
$$\left.\times\left(2v_x\frac{\partial v_x}{\partial x} + v_y\frac{\partial v_x}{\partial y} + v_z\frac{\partial v_x}{\partial z} + v_x\frac{\partial v_y}{\partial y} + v_x\frac{\partial v_z}{\partial z}\right)\right]dz. \qquad (41)$$
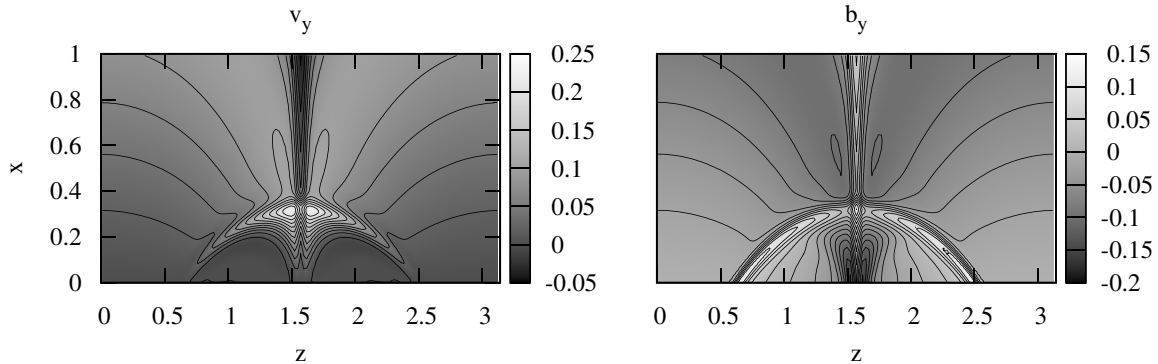
Figure 2. Components v_y and b_y at time $\tau = 10$ in the case of Alfvénic perturbations, with isolines.

4. NUMERICAL RESULTS

In the following, we describe the results obtained in numerical simulations. We first consider the case of the Alfvénic perturbation.

4.1. Alfvénic Perturbation

In this case, the velocity component directed perpendicularly to the plane of the simulation, v_y, is directly excited by boundary conditions at the lower boundary. Magnetic lines are locally bent in the y direction and a non-vanishing b_y magnetic field component is generated at $x = 0$. The y components of the velocity and magnetic field represent the main Alfvénic wave component of the fluctuation generated at the lower boundary. Such a wave propagates inside the domain following magnetic lines. In Figure 2 the velocity v_y and magnetic field b_y components are plotted at the time $\tau = 10$. At that time, the perturbation continuously produced at $x = 0$ has filled the whole spatial domain. We can discriminate two different behaviors of fluctuations in open or closed fieldline regions. In the former regions, fluctuations cross the domain in the upward direction and eventually exit from the top. We verified that no significant reflection takes place at the upper boundary; this shows that an open boundary is well reproduced by the method of characteristics. Open fieldline regions are separated in the lower part of the domain, but they come in contact in the upper part through the vertical separatrix, which is above the X-point (see Figure 1); thus, upward-propagating waves completely fill the upper part of the domain. In this region, v_y and b_y appear to be anticorrelated (Figure 2), as required for Alfvén waves propagating in the direction of the background magnetic field. Since the Alfvén speed is not uniform, the wave propagates faster at the flanks than in the middle of the domain, thus producing phase-mixing (Heyvaerts & Priest 1983). This can be seen in Figure 2, where wavefronts (indicated by the isolines of v_y and b_y), which are nearly horizontal in the lower domain, approach one another and become nearly vertical in the upper central part. This effect increases the wavevector component perpendicular to the background magnetic field; $\mathbf{b}^{(0)}$ is nearly vertical at large x, so small scales in the horizontal z direction are produced in the upper part of the domain. This effect is more significant around the vertical separatrix, because fluctuations traveling in this region have passed near the X-point, where the Alfvén velocity vanishes. As a result, small scales in the upper part of the domain are concentrated in the central region around the separatrix.

In closed fieldline regions, the perturbation generated at the lower boundary remains confined beneath the separatrices and cannot propagate higher. In this region, waves coming from different parts of the lower boundary propagate along magnetic lines in opposite directions. In these waves v_y and b_y can be either positively correlated or anticorrelated, according to the sense of propagation. As a consequence, no particular correlation between v_y and b_y is observed in the closed fieldline regions, where these two kinds of waves are superposed (Figure 2). However, all waves propagating close to the curved separatrices pass close to the X-point where the Alfvén velocity vanishes and undergo an intense phase-mixing. Then, small scales form around the separatrices that are also in closed fieldline regions. This phenomenon had been previously reported by McLaughlin et al. (2010).

The formation of small scales can be visualized by plotting the spatial distribution of the heat-source terms P_η and P_ν due to resistive and viscous dissipation, as defined in Equation (35). In fact, dissipation becomes stronger at locations where small scales are present. In Figure 3, $P_\eta(x, z, \tau)$ and $P_\nu(x, z, \tau)$ are plotted at the time $\tau = 10$. As expected, most of the dissipated power is concentrated around the four separatrices. Around the upper separatrix we found that $P_\eta \simeq P_\nu$, which is a consequence of the velocity–magnetic field correlation ($v_y \simeq -b_y$) found in that region, along with the choice that viscosity ν and resistivity η are equal. On the contrary, around the other separatrices v_y and b_y are no longer correlated, so P_η and P_ν can be different. In particular, we found that P_η is slightly larger than P_ν.

To obtain a quantitative evaluation of the dissipated power, we calculated the integrated dissipated power $w_\eta(\tau)$, $w_\nu(\tau)$ defined in Equation (36), and their sum $w(\tau) = w_\eta(\tau) + w_\nu(\tau)$. These quantities are plotted in Figure 4 as functions of time τ. The dissipated power is initially null and grows until the time $\tau \sim 3$, when it reaches a quasi-stationary state where it oscillates around a mean value $\langle w \rangle \simeq 0.0017$. Comparing this value with the mean input energy flux $\langle \Phi_0 \rangle$ calculated at the lower boundary $x = 0$, we found that $\langle w \rangle / \langle \Phi_0 \rangle \sim 0.15$ for $\nu = \eta = 10^{-2}$, whereas $\langle w \rangle / \langle \Phi_0 \rangle \sim 0.1$ for $\nu = \eta = 10^{-3}$. Then, for the considered values of the dissipative coefficient, about 10% of the power that enters the domain in form of Alfvén waves is dissipated inside the domain (i.e., at very low levels in the corona). However, the above results do not allow us to obtain an evaluation of the ratio $\langle w \rangle / \langle \Phi_0 \rangle$ for more realistic values of dissipative coefficient, which are much lower in the coronal plasma than the values we used in the simulation. Comparing resistive and viscous dissipated power, we see that $w_\eta(\tau) > w_\nu(\tau)$ (i.e., more magnetic energy is dissipated than kinetic energy). Within the linear approximation we can assume that velocity and magnetic field perturbations are polarized along the y direction. Since the equilibrium magnetic field $\mathbf{b}^{(0)}$
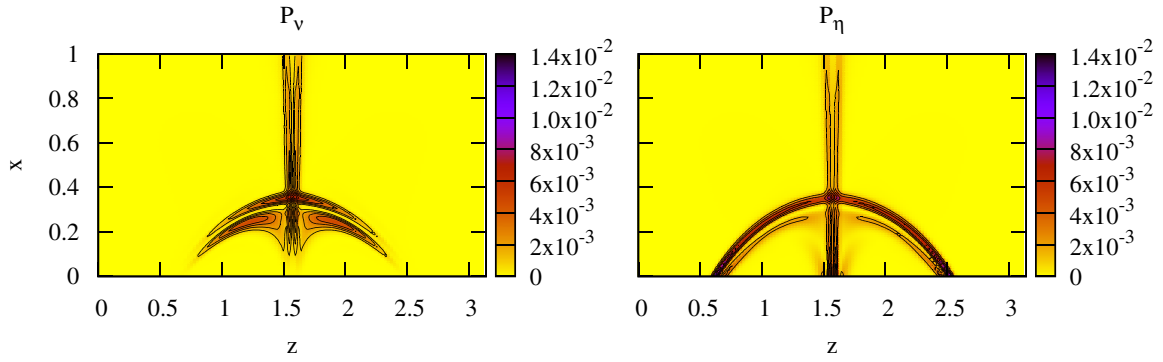
Figure 3. Dissipated power per unit volume due to viscosity P_ν (left panel) and resistivity P_η (right panel) in the xz plane at the time $\tau = 10$ for the Alfvénic perturbation.

(A color version of this figure is available in the online journal.)

is a current-free field, dissipated powers in the region around separatrices can be estimated by

$$P_\eta \simeq \eta(\nabla b_y)^2 \sim \eta\frac{(\delta b_y)^2}{\ell^2}, \quad P_\nu \simeq \nu(\nabla v_y)^2 \sim \nu\frac{(\delta v_y)^2}{\ell^2}, \tag{42}$$

where ℓ is the dissipative scale and δb_y and δv_y are local amplitudes of magnetic field and velocity fluctuations, respectively. Around the upper separatrix, only upward-propagating waves are present with $\delta b_y \simeq \delta v_y$. In contrast, around the lower separatrices where waves propagate in both senses, we observe that $\delta b_y > \delta v_y$. Thus, the slight unbalance between $w_\eta(\tau)$ and $w_\nu(\tau)$ could be due to lack of fluctuating magnetic and kinetic energy equipartition in the region of closed magnetic fieldlines.

In order to illustrate the presence of small scales in the fluctuations leaving the domain from the upper boundary, we calculated the spectrum of the velocity component v_y. As explained previously, we expect that small-scale formation due to phase-mixing takes place only in the direction perpendicular to $\mathbf{b}^{(0)}$ (i.e., mainly in the horizontal direction). Thus, we calculated a 1D spectrum giving the energy distribution at the various scales in the z direction. The velocity y component calculated at the upper boundary $x = 1$ is expanded in the Fourier series

$$v_y(1, z, \tau) = \sum_{k_z} \hat{v}_y(k_z, \tau)e^{ik_z z}. \tag{43}$$

The time-dependent spectrum is given by $|\hat{v}_y(k_z, \tau)|^2$. We found that the shape of such a spectrum varies quasi-periodically in time according to the instantaneous value of the wave phase. For this reason it is suitable to consider a spectrum averaged in time over a wave period $T = 2\pi/\omega$:

$$e_{v_y}(k_z) = \frac{1}{T}\int_T |\hat{v}_y(k_z, \tau)|^2 d\tau. \tag{44}$$

The time-averaged velocity spectrum is plotted in Figure 5 in logarithmic scale. It can be seen that $e_{v_y}(k_z)$ follows a power law remarkably well, up to wavevectors $k_z \sim 30$. For larger wavevectors the spectrum becomes curved, which is probably due to dissipation. In the power-law range, the spectrum is well fitted by a law $\propto k_z^{-2.3}$. A very similar spectrum has also been found for the magnetic fluctuation b_y. Thus, the effect of the inhomogeneous magnetic field $\mathbf{b}^{(0)}$ where the Alfvénic fluctuation propagates is to create a power-law spectrum in the initially uniform perturbation. We point out that the power-law
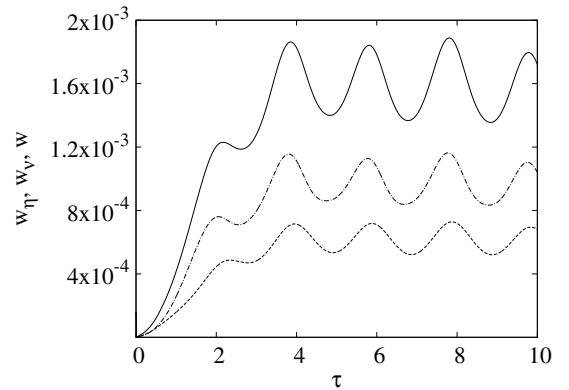

Figure 4. Integrated dissipated power due to viscosity w_ν (dashed line), to resistivity w_η (dash-dotted line), and total w (solid line), plotted as functions of time for the Alfvénic perturbation.
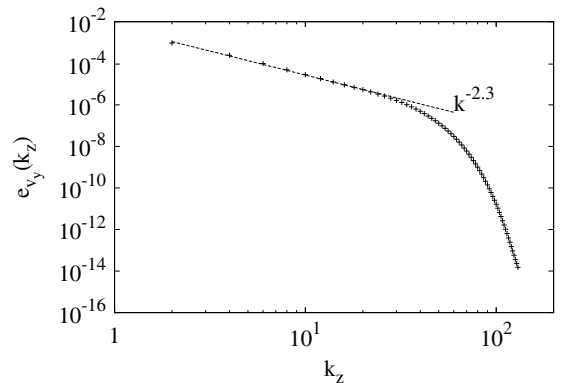

Figure 5. Time-averaged velocity y-component spectrum $e_{v_y}(k_z)$ calculated at $x = 1$ for the Alfvénic perturbation (crosses), and a power-law function that fits the spectrum in the low-wavenumber range (dashed line) are plotted in logarithmic scale.

spectrum we found is steeper than the Kolmogorov spectrum. We note that the same result, with a similar value for the spectral slope, has also been found by Malara (2013) in a model based on the WKB approximation, in which small-wavelength Alfvén waves propagate along magnetic lines at the local Alfvén speed. McLaughlin et al. (2010) showed that a small-amplitude Alfvén wave in a 2D equilibrium magnetic field with a uniform density follows magnetic lines with the local Alfvén speed, regardless of its wavelength. Thus, the formation in our simulation of a spectrum similar to that found in the WKB limit was expected.
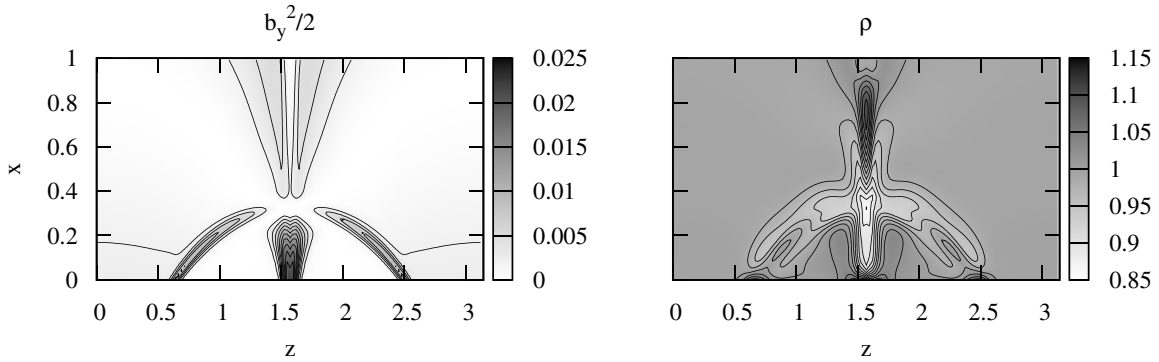
Figure 6. Magnetic pressure p_M associated with the Alfvénic perturbation (left panel) and density ρ (right panel) calculated at the time $\tau = 8.5$.

The wave amplitude is small with respect to the background magnetic field, being $b_y/b^{(0)} \sim 0.1$. Thus, it could be expected that nonlinear effects depending on the square of the wave amplitude, such as the generation of compressive fluctuations, should be negligible when compared with the Alfvénic fluctuation. However, magnetic pressure gradients could locally be large enough to drive significant compressible fluctuations. This happens around separatrices, because of the presence of small-scale structures in the wave profile. The Laplace force associated with the total magnetic field $\mathbf{b} = [\mathbf{b}^{(0)} + b_y\mathbf{e}_y]$ is $\mathbf{f} = (\nabla \times \mathbf{b}) \times \mathbf{b}$. Taking into account the condition $\nabla \times \mathbf{b}^{(0)} = 0$, $\mathbf{f}$ has the form

$$\mathbf{f} = -\frac{\partial}{\partial x}\left(\frac{b_y^2}{2}\right)\mathbf{e}_x + \left(b_x^{(0)}\frac{\partial b_y}{\partial x} + b_z^{(0)}\frac{\partial b_y}{\partial z}\right)\mathbf{e}_y - \frac{\partial}{\partial z}\left(\frac{b_y^2}{2}\right)\mathbf{e}_z. \tag{45}$$

Thus, the components of $\mathbf{f}$ in the xz plane are opposite to the magnetic pressure gradient associated with the perturbation field b_y. These components can reach significant values at locations where small scales form (i.e., around the separatrices). In Figure 6 the magnetic pressure $p_M = b_y^2/2$ due to the perturbation of the magnetic field component b_y, and the density ρ are plotted at time $\tau = 8.5$ in the left and right panels, respectively. We observe an increase of magnetic pressure on both sides of the vertical separatrix above the X-point, with lower values of p_M in between. This is due to the accumulation of wavefronts of the Alfvén wave caused by phase-mixing. This results in strong localized gradients of p_M that push the fluid toward the separatrix from both sides. The result is the formation of a dense, vertically elongated "bubble" localized on the separatrix, where the density reaches values up to $\sim$10–15% larger than the unperturbed value. This compressive structure can be seen in the right panel of Figure 6. The compressive perturbation evolves in time, propagating upward, pushed by the magnetic pressure of the Alfvén wave. This time evolution is represented in Figure 7, where the density profile is plotted as a function of x along the separatrix at $z = \pi/2$ for different times. At the time $\tau = 8$ a maximum of density, where ρ reaches the value $\simeq 1.12$ is located above the X-point, at $x \simeq 0.59$. This fluctuation propagates upward with a speed $\sim$0.3–0.4 (in dimensionless units), which increases with increasing x, whereas the fluctuation amplitude slightly decreases. The Alfvén velocity on the separatrix at $x = 1$ is $c_A \simeq 0.26$, even if it increases on the two sides of the separatrix. Eventually, the density perturbation exits the domain through the boundary $x = 1$, while a new compression forms above the X-point (time $\tau = 9.5$). We verified that the period of the compressive fluctuations is around two, which is one half the
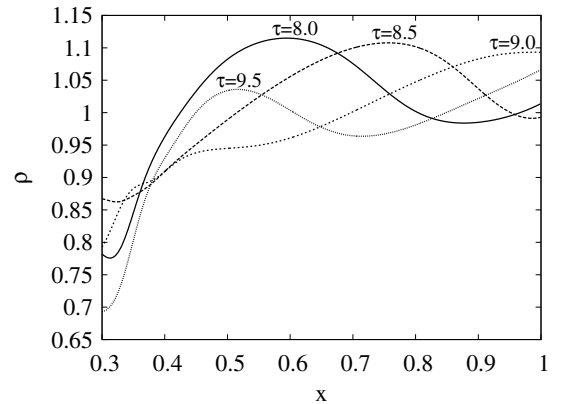

Figure 7. Density profiles as functions of x along the vertical separatrix $z = \pi/2$ at different times.

period of the Alfvénic perturbation. Summarizing, in the vicinity of the separatrix nonlinear effects generate density fluctuations with an amplitude $\delta\rho/\rho$ of the same order as the amplitude of the Alfvén wave. Such fluctuations are driven by the Alfvén wave magnetic pressure gradient and propagate along the magnetic field at a speed comparable with the Alfvén velocity.

4.2. Magnetosonic Perturbation

In this case a velocity perturbation polarized in the z direction is imposed at the lower boundary. This motion locally distorts the equilibrium field magnetic lines, generating a perturbation of both x and z magnetic field components. At variance with the previous case, no perturbation y components are generated. Thus, the perturbation produced at the boundary belongs to the magnetosonic mode. We shall see that the behavior of the system is different from the previous case, with a more important role played by the X-point.

In Figure 8 the velocity components v_y and v_z are plotted at the time $\tau = 2$. It can be seen that the distribution of the velocity field is no longer symmetric. Moreover, the spatial distribution of $\mathbf{v}$ is smoother and more isotropic than in the Alfvénic case. No small scales appear to be present in the upper part of the domain (i.e., in the region where the perturbation leaves the domain). We then calculated the time-averaged spectra of the x and z components of the velocity and magnetic field. In the same way as the Alfvénic perturbation case, these spectra are calculated using the profiles of the above quantities taken along the upper boundary $x = 1$. The averaged spectra e_{v_x}, e_{v_z}, e_{b_x}, and e_{b_z} are plotted in Figure 9. All such spectra are much steeper than those found for the Alfvénic perturbation. We can
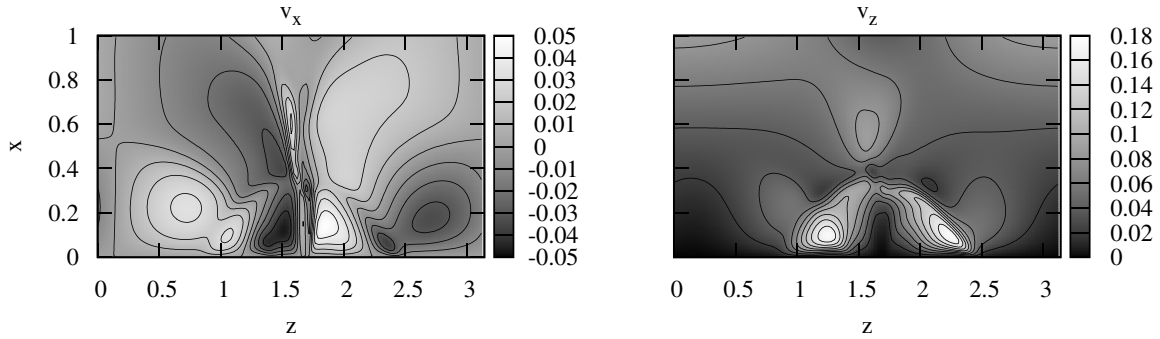
Figure 8. Velocity components v_x and v_z at time $\tau = 2$ for the magnetosonic perturbation.
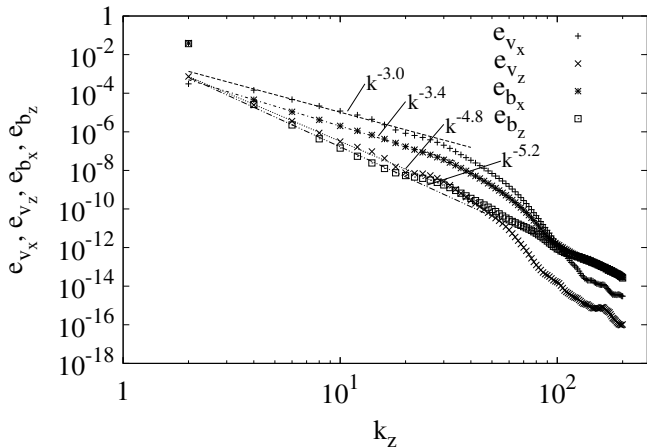

Figure 9. Velocity $e_{v_x}(k_z)$ (crosses), $e_{v_z}(k_z)$ ("x" symbols), and magnetic field $e_{b_x}(k_z)$ (stars), $e_{b_z}(k_z)$ (squares). Time-averaged spectra calculated at $x = 1$ are plotted with power laws fits (lines).

conclude that no relevant small scales are present in the magnetosonic perturbations that leave the domain through the upper boundary.

Indeed, small scales are present in the domain, but only in a limited region around the X-point. This confirms a finding by McLaughlin et al. (2010), who reported that magnetosonic perturbations are diffracted by the background inhomogeneities and, in the presence of an X-point, wrap around it locally generating small scales. Because of the imposed v_z at the lower boundary and the frozen-in law, magnetic fieldlines at the lower boundary are forced to follow the oscillatory motion at the base. We remember that the magnetic field is not imposed at the boundary, but is calculated using a method of projected characteristics that takes into account physical conditions imposed for the velocity. The oscillation of the value of v_z along the lower boundary causes a distortion of the magnetic structure, which is also oscillatory. In Figure 10 magnetic field lines are plotted at two different times. Each plot is obtained by drawing the isolines of the vector potential $A(x, z)$. In Appendix B we describe the method we used to calculate $A(x, z)$. By comparing Figure 1 we can see the distortion of the magnetic lines generated by the perturbation. In particular, the separatrices crossing at the X-point have collapsed—they no longer form right angles in the distorted configuration of Figure 10. This implies that a current directed along the y direction is localized at the X-point. The current density component $j_y = \partial b_x/\partial z - \partial b_z/\partial x$ is plotted in Figure 11 at the time $\tau = 2$ (corresponding to the left panel of Figure 10). This figure represents a zoom of the region

around the X-point. We can see that j_y has a maximum at the X-point and it is flattened along an oblique direction, which is between separatrices. Such an elongated X-point becomes a site of magnetic reconnection. The presence of magnetic reconnection can be revealed by plotting the vorticity y component $\omega_y = \partial v_x/\partial z - \partial v_z/\partial x$ (Figure 11, right panel); ω_y displays a quadrupolar structure that is typical of magnetic reconnection (Matthaeus 1982): two opposite inflows carry magnetic flux that reconnects at the X-point and is carried away by two opposite outflows. Thus, the magnetic field distortion produced by the perturbation works as a trigger for the magnetic reconnection. This goes on until the change of sign in the velocity v_z at the base pulls fieldlines in the opposite direction, causing the X-point to become currentless and stopping the reconnection for a moment. The distortion continues until the configuration shown in the right panel of Figure 10 is formed, which is specular to the previous one. In this new configuration reconnection starts again, but is opposite to the previous case—previous inflows turn into outflows, and vice versa. This cycle of reconnection reversals continues periodically. In our simulation reconnection is oscillatory in time, which is a consequence of the periodic motion imposed at the lower boundary. The presence of oscillatory reconnection in a magnetic X-point perturbed by a magnetosonic wave was previously reported by McLaughlin et al. (2009). These authors considered an X-point at the center of a cylindrical domain, where a single δ-like magnetosonic pulse coming from the boundary converges to the X-point. The pulse generates a sequence of alternate reconnections decaying in time that are caused by the increase of kinetic pressure in the outflow regions of the reconnection. In our simulation, we considered magnetosonic waves with a well-defined frequency, so that oscillatory reconnection goes on indefinitely without decaying. Moreover, our results show that this phenomenon can also act in more general (less symmetrical) configurations, provided that an initially potential X-point is solicited by some perturbation polarized in the same plane as the background magnetic field.

5. CONCLUSIONS

In this paper we studied the propagation of MHD waves in the lower layers of a coronal hole, through 2D MHD numerical simulations. Such waves are supposed to be generated by photospheric motions and propagate upward reaching higher regions of the corona and the solar wind. The main motivation is to study the formation of small scales in fluctuations, as a consequence of their interaction with features of the inhomogeneous background magnetic field, such as separatrices and X-points. Indeed, although a coronal hole is characterized by
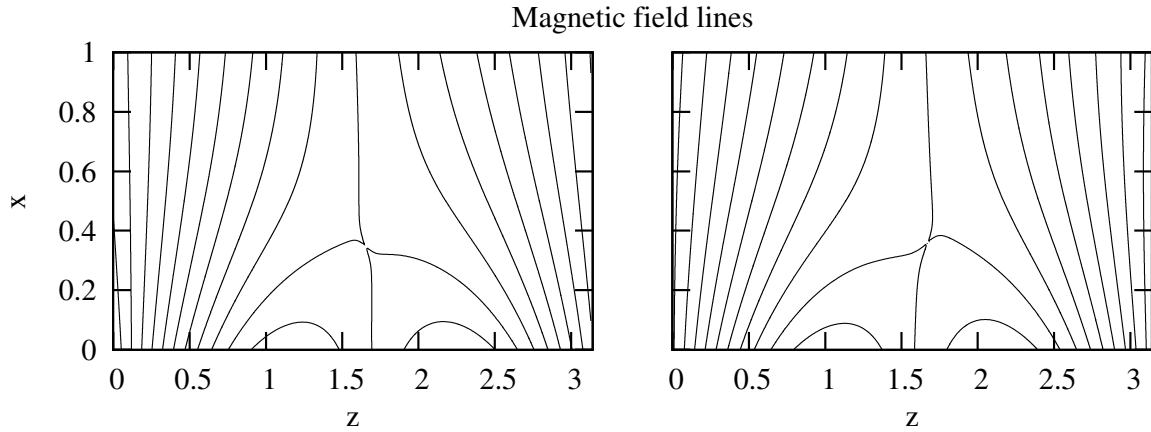
Magnetic field lines

Figure 10. Magnetic field lines in the xz plane at times $\tau = 2$ (left panel) and $\tau = 3.5$ (right panel).
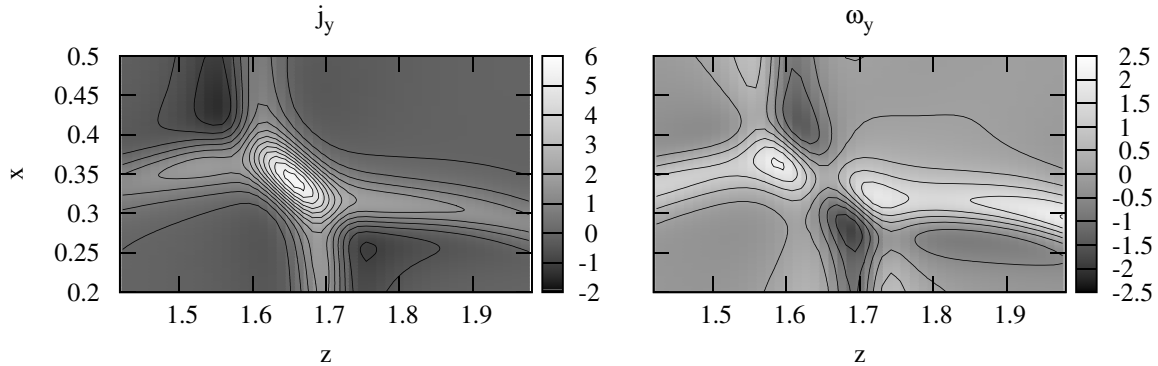

Figure 11. Current component j_y (left panel) and vorticity component ω_y (right panel) in the xz plane around the X-point at the time $\tau = 2$.

a dominant magnetic polarity, magnetograms have revealed the presence of several regions of opposite polarity (Zhang et al. 2006; Ito et al. 2010), with a typical size of the order of 10^4 km. This suggests that at low altitudes the magnetic field has a complex structure containing both open and closed fieldlines, the latter connecting regions of opposite polarity at the base. When a fluctuation crosses such a complex structure, small scales are generated. These effects have been neglected in the models of solar wind acceleration, where only large-scale inhomogeneities due to vertical stratification and spherical expansion have been included.

We considered magnetic structures with a typical size $L = 10^4$ km $\ll 1 R_\odot$. Then, in our model we neglected curvature effects due to the spherical geometry, instead using a simpler Cartesian geometry. The equilibrium magnetic field we considered tries to reproduce the above observational features—it is a simple inhomogeneous 2D current-free field, whose vertical component b_x changes sign when moving along the base $x = 0$. In the model there are both open and closed fieldlines at small x, while only open fieldlines with a single polarity are present at large x. The magnetic structure contains separatrices that intersect at an X-point; the separatrices and the X-point play a key role in the dynamics of perturbations. The equilibrium density is supposed to be uniform. The scale height H_ρ of the density in the corona can be estimated by assuming a uniform temperature and an equilibrium between gravity, a pressure gradient, and a uniform temperature, $H_\rho \simeq \kappa_B T^{(0)}/(m_p g)$, where κ_B is the Boltzmann constant, m_p the proton mass, $g \simeq 2.74 \times 10^4$ cm s^{-2} the surface gravity of the Sun, and $T^{(0)} \simeq 10^6$ K. Using these values, we find $H_\rho \simeq 3 \times 10^4$ km, which is larger than the verti-

cal size L of our domain. Thus, a uniform density is a reasonable approximation.

Fluctuations are produced by imposing a velocity v_y or v_z at the base $x = 0$ of the domain. This is intended to represent movements of lower denser layers of the solar atmosphere. In consequence of the frozen-in condition, magnetic fieldlines are carried by these motions, thus generating MHD waves that propagate from the base into the domain. The time evolution of magnetic field, density, and pressure at the base has been calculated consistently with MHD equations using a method of projected characteristics. The same method allows perturbations to exit without reflection through the upper boundary $x = 1$. Since the background magnetic field is 2D, it is possible to distinguish between Alfvénic and magnetosonic perturbations, according to the polarization (y or xz) of the generated fluctuations.

In the case of Alfvénic perturbation, we found that the formation of small-scale structures mainly takes place along the separatrices. This holds for both the lower separatrices, where trapped perturbations propagate back and forth, and for the upper separatrix in the open fieldline region, where fluctuations leave the domain propagating upward. Small scales form both in the magnetic field and in the velocity perturbation. The generation of small scales along the separatrices confirms the results of previous studies, which were carried out using various approaches (analytical, WKB, simulation) concerning Alfvén wave propagation around an X-point (see, e.g., McLaughlin et al. 2010 for a review). The separatrices are also the places where the energy carried by the waves is transformed into heat through dissipative effects. During the time evolution the dissipated power reaches a quasi-stationary state after an initial

transient. In this quasi-stationary situation we estimated that $\sim$10% of the energy flux entering from the base is dissipated in the domain and the rest is carried out with the waves. This percentage decreases with decreasing dissipative coefficients, which in our simulations are necessarily much higher than in the coronal plasma. A more detailed analysis of this point is left for a future work. On the other hand, we can expect that if the domain had a larger extension in the x direction, the ratio of dissipated to incoming power would be larger. In our simulation more power is dissipated by resistivity than by viscosity; this difference is due to the behavior of waves trapped in the region of closed fieldlines, where magnetic perturbations are larger than velocity perturbations. The dominance of magnetic perturbations has been observed for low-frequency perturbations in models of turbulence in coronal loops (Nigro et al. 2004; Buchlin et al. 2007). As in our case, in these models a fluctuating velocity is imposed at the boundaries, while outgoing perturbations are free to leave the spatial domain. The observed unbalance between velocity and magnetic field perturbations in closed fieldline regions of our model could be ascribed to a mechanism similar to that found in the models by Nigro et al. (2004) and Buchlin et al. (2007), although the excitation of "in phase" fluctuations at the footpoints of closed fieldlines could also play a role in determining the excess of magnetic fluctuations.

In analyzing the spectrum of the perturbation exiting from the top, we found that the energy is distributed as a power law $\propto k_z^{-2.3}$, at least at scales sufficiently large to neglect dissipative effects. k_z represents the main component of the wavevector, which is essentially perpendicular to $\mathbf{b}^{(0)}$. Then, the interaction of an initially spatially uniform Alfvénic perturbation with the background inhomogeneity produces an anisotropic power-law spectrum that mainly extends in the direction perpendicular to the magnetic field. This spectrum forms at low altitudes in the corona—at $X = L = 10^4$ km above the coronal base the spectrum is completely formed. These results largely confirm what has been found by Malara et al. (2012) and Malara (2013). However, while these authors employed a WKB approximation in a 3D configuration, our results are based on a direct MHD simulation in a 2D equilibrium. The above features of the spectrum are reminiscent of what happens in MHD turbulence, where nonlinear couplings generate power-law spectra with an energy cascade that mainly flows in the direction perpendicular to the mean magnetic field (e.g., Shebalin et al. 1983; Carbone & Veltri 1990). In the present model this anisotropy is generated by the coupling between the perturbation and the inhomogeneous background, instead of nonlinear effects. However, the slope $\alpha \simeq 2.3$ of the perturbation spectrum that we find is definitely larger than what is typically found in turbulence (e.g., 1.5 or 1.66 for a Kraichnan or a Kolmogorov spectrum, respectively). Thus, the present model cannot account for the formation of a fully developed spectrum. However, models studying the evolution of fluctuations from the corona to the solar wind, or the solar wind acceleration by dissipation of wave energy should take the phenomenon we studied here into account. For instance, Verdini et al. (2009) presented a model of turbulence formation in the sub-Alfvénic solar wind, where Alfvén waves on large scales are injected at the base and partially reflected by the vertical stratification. Although a turbulence spectrum forms as a consequence of nonlinear wave–wave interactions, the produced heat seems to be deposited at greater distances than what is needed to sustain the background wind. Our model suggests that upward-propagating waves start forming small scales at very low altitudes. Such a phenomenon can decrease

the altitude of heat deposition, thus leading to a better agreement between the results of the turbulence model and the background wind structure.

The relative amplitude of perturbations we considered is low ($\delta v/c_A \sim 10^{-1}$), so that nonlinear effects should be mostly negligible. Nevertheless, the magnetic pressure gradient associated with the perturbation can locally reach larger values at locations where small scales form. As a consequence, in the vicinity of the vertical separatrix we observed the formation of density fluctuations with a relative amplitude ($\delta\rho/\rho \sim 10^{-1}$) comparable with that of the Alfvén wave. These fluctuations are sort of localized "bubbles" that propagate upward along the separatrix at a speed ($\sim$100 km s^{-1}) comparable with the local Alvén velocity pushed by the magnetic pressure of the Alfvén wave. The presence of density fluctuations in coronal holes with a period of approximately six minutes has been revealed by Ofman et al. (1997). DeForest & Gurman (1998) found compressive waves in polar plumes with waveperiods of $\sim$10 minutes, propagating upward at a speed $\sim$75–150 km s^{-1}, where the density fluctuation is 5%–10% of the background value, interpreted as slow magnetosonic fluctuations (Ofman et al. 1999). On the other hand, magnetograms reveal the presence of small regions of magnetic polarity opposite the dominant plume polarity located all around the plume footpoint (DeForest et al. 1997). This could give rise to magnetic separatrix surfaces associated with the plume boundary. Our model suggests an alternative interpretation of the observed density fluctuations—namely, compressive waves, nonlinearly driven by Alfvénic fluctuations, which propagate upward along such magnetic separatrices. Finally, we noted an analogy between our magnetic structure and that of pseudostreamers (Wang et al. 2012). A certain activity has been observed in the form of faint density structures radially propagating along pseudostreamers up to distances $\sim$3$R_\odot$ (Wang et al. 2007). The similarity with our model would suggest that such structures could be generated by steep magnetic pressure gradients of Alfvén waves that concentrate around the magnetic separatrix. However, since pseudostreamers can extend up to about few solar radii density, stratification and spherical geometry are no longer negligible. These effects could somehow modify the wave dynamics with respect to that found in our model.

The phenomenology of magnetosonic fluctuations is completely different. First, no relevant small-scale formation is observed in the waves that leave the domain through the upper boundary: spectra of velocity and magnetic field components at $x = 1$ are much steeper than for Alfvénic fluctuations, with slopes ranging from $\simeq -3.0$ to $\simeq -5.2$. We can conclude that only Alfvénic fluctuations contribute to the small-scale formation in waves that leave the domain, at least in the considered 2D configuration. However, in the magnetosonic case, small scales do actually form and dissipation takes place, but only around the X-point. The magnetic field is perturbed by the magnetosonic fluctuation so that an elongated current j_y forms at the initially potential X-point; the separatrices collapse and reconnection starts. In this scenario, fluctuations work as a trigger for reconnection. With increasing time, the motion at the base is reversed until magnetic lines at the X-point reach a configuration specular to the previous one: the reconnection pattern is reversed, with outflows turned into inflows, and vice versa. The oscillatory motion imposed at the base gives rise to an oscillatory reconnection. The phenomenon of oscillatory reconnection has been observed by Murray et al. (2009) in simulations of an emerging flux tube within a coronal hole. McLaughlin et al. (2009) studied oscillatory reconnection when a magnetosonic pulse propagates

on a potential X-point. However, while these authors considered a single δ-like pulse generating a self-sustained time-decaying sequence of reconnections, in our simulation alternate reconnection indefinitely goes on, driven by a continuous wave injection. Moreover, the configuration studied by McLaughlin et al. (2009) is more particular than ours, since these authors considered a cylindrically symmetric pulse converging toward the X-point. In this respect, we can say that our results extend the findings by McLaughlin et al. (2009) to more general configurations that are not necessarily constrained by cylindrical symmetry assumptions. Oscillatory reconnection has been invoked (Murray et al. 2009) to explain oscillatory emission observed during flares (e.g., Mitra-Kraev et al. 2005; McAteer et al. 2005; Inglis et al. 2008), as well as swaying outflow jets observed above emitting loops (Cirtain et al. 2007; Shibata et al. 2007). Our results indicate that oscillatory reconnection should be a general phenomenon taking place every time a current-free X-point is stressed by a quasi-periodic perturbation.

Despite its simplicity, we believe that the present model has allowed us to gain some insight in the mechanism of small-scale formation into perturbations that propagate in the lower layers of a coronal hole. Possible improvements that we are planning for future work include both the extension to a more complex 3D structure and a more realistic representation of motions at the coronal base, which takes into account the observed temporal spectrum of photospheric motions.

APPENDIX A

THE METHOD OF PROJECTED CHARACTERISTICS

The method of characteristics can be used to build boundary conditions that are consistent with the hyperbolic structure of fluid or MHD equations. It is based on the decomposition of solutions of the Equations (28)–(31) into characteristic modes that cross the domain boundary propagating from inside to outside, or the reverse. We employed a version of the method that has been formulated by Sun et al. (1995) and was used to simulate the entrance and exit of Alfvénic perturbations both in a large-scale coronal model (Grappin et al. 2000) and in an equilibrium structure with an X-point (Landi et al. 2005). In these cases, the entrance of Alfvén waves was obtained by imposing the amplitude of incoming perturbations at the boundary. In the present case we follow a different approach (i.e., the input of perturbations is obtained by imposing a time-dependent velocity field on the lower boundary $x = 0$). We use the method of projected characteristics to deduce the time evolution of the other physical quantities (density, pressure, and magnetic field) at the same boundary in a way that is consistent with the MHD equations. At the upper boundary $x = 1$, the method is used to simulate the free exit of perturbations by imposing that no perturbation enters the domain through that boundary (Grappin et al. 2000; Landi et al. 2005).

We write the compressible, non-ideal, MHD Equations (28)–(31) separating the terms containing first-order derivatives with respect to x from the other terms:

$$\frac{\partial U_i}{\partial \tau} + A_{ij} \frac{\partial U_j}{\partial x} + T_i = 0, \quad i = 1, \ldots, 7, \tag{A1}$$

where $\mathbf{U}^t = \left(\rho, v_x, v_y, v_z, b_y, b_z, p \right)$ and the vector $\mathbf{T}$ contain all the terms with derivatives with respect to y and z and the non-ideal terms. Hereafter, summation over dummy indices is understood. We eliminated the equation for b_x in the system (A1) because we calculate its value at the boundaries $x = 0$ and $x = 1$ by using the divergence free condition. The matrix A has the following form:

$$A = \begin{pmatrix} v_x & \rho & 0 & 0 & 0 & 0 & 0 \\ 0 & v_x & 0 & 0 & \frac{b_y}{\rho} & \frac{b_z}{\rho} & \frac{1}{\rho} \\ 0 & 0 & v_x & 0 & -\frac{b_x}{\rho} & 0 & 0 \\ 0 & 0 & 0 & v_x & 0 & -\frac{b_x}{\rho} & 0 \\ 0 & b_y & -b_x & 0 & v_x & 0 & 0 \\ 0 & b_z & 0 & -b_x & 0 & v_x & 0 \\ 0 & \gamma p & 0 & 0 & 0 & 0 & v_x \end{pmatrix}.$$

The eigenvalues of the matrix A are: $\lambda^{(1)} = v_x$, $\lambda^{(2)} = v_x + c_{ax}$, $\lambda^{(3)} = v_x + c_f$, $\lambda^{(4)} = v_x + c_s$, $\lambda^{(5)} = v_x - c_{ax}$, $\lambda^{(6)} = v_x - c_f$, $\lambda^{(7)} = v_x - c_s$, where $c_{ax} = b_x/\sqrt{\rho}$ is the Alfvén speed along the x direction, $c_f = 1/\sqrt{2}(\sqrt{(c_a^2 + a^2) + 1/2\sqrt{(c_a^2 + a^2) - 4c_{ax}^2 a^2}})$ and $c_s = 1/\sqrt{2}(\sqrt{(c_a^2 + a^2) - 1/2\sqrt{(c_a^2 + a^2) - 4c_{ax}^2 a^2}})$ are the fast and slow magnetosonic speeds, with $a^2 = \sqrt{\gamma P/\rho}$ and $c_a^2 = b^2/\rho$. The eigenvalues $\lambda^{(k)}$ represent the propagation velocities of the seven different waves (Alfvén, fast and slow magnetosonic, and entropy waves) crossing the boundary in both senses. For each of the two boundaries we distinguish between *incoming perturbations* (corresponding to positive $\lambda^{(k)}$ at $x = 0$, or negative $\lambda^{(k)}$ at $x = 1$) and *outgoing perturbations* (corresponding to negative $\lambda^{(k)}$ at $x = 0$, or positive $\lambda^{(k)}$ at $x = 1$).

We indicate by $\xi^{(k)}$ and $\eta^{(k)}$ the right and left eigenvector of the matrix A corresponding to the kth eigenvalue $\lambda^{(k)}$:

$$A_{ij}\xi_j{}^{(k)} = \lambda^{(k)}\xi_i{}^{(k)} \quad \eta_i{}^{(k)}A_{ij} = \lambda^{(k)}\eta_j{}^{(k)} \quad k = 1, \ldots, 7, \tag{A2}$$

where no summation is to be intended over the upper index in parenthesis (k). A right (left) eigenvector and a left (right) eigenvector corresponding to different eigenvalues are mutually orthogonal. Moreover, we choose to normalize eigenvectors so that:

$$\xi_i{}^{(k)}\eta_i{}^{(l)} = \delta_{kl}. \tag{A3}$$

In the following we illustrate the procedure in the most general case, in which all magnetic field components are nonvanishing at the given grid point on the boundary. The two particular cases in which $b_x = 0$ or $b_\perp = \left(b_y^2 + b_z^2\right)^{1/2} = 0$ have been treated in a similar way. The explicit expressions of left eigenvectors are:

$$\eta^{(1)} = \left(\frac{1}{\rho}, 0, 0, 0, 0, 0, -\frac{1}{\gamma p}\right) \tag{A4}$$

$$\eta^{(2)} = \left(0, 0, -\sigma\frac{\sqrt{\rho}b_z}{2b_\perp^2}, \sigma\frac{\sqrt{\rho}b_y}{2b_\perp^2}, \frac{b_z}{2b_\perp^2}, -\frac{b_y}{2b_\perp^2}, 0\right) \tag{A5}$$

$$\eta^{(3)} = \left(0, 0, \sigma\frac{\sqrt{\rho}b_z}{2b_\perp^2}, -\sigma\frac{\sqrt{\rho}b_y}{2b_\perp^2}, \frac{b_z}{2b_\perp^2}, -\frac{b_y}{2b_\perp^2}, 0\right) \tag{A6}$$

$$\eta^{(4)} = \left(0, \frac{1}{2\gamma_f c_f}, -\frac{b_y}{2b_x\alpha_f\gamma_f c_f}, -\frac{b_z}{2b_x\alpha_f\gamma_f c_f}, \frac{b_y}{2b_x^2\alpha_f\gamma_f}, \frac{b_z}{2b_x^2\alpha_f\gamma_f}, \frac{1}{2\rho\gamma_f c_f^2}\right) \tag{A7}$$

$$\eta^{(5)} = \left(0, -\frac{1}{2\gamma_f c_f}, \frac{b_y}{2b_x\alpha_f\gamma_f c_f}, \frac{b_z}{2b_x\alpha_f\gamma_f c_f}, \frac{b_y}{2b_x^2\alpha_f\gamma_f}, \frac{b_z}{2b_x^2\alpha_f\gamma_f}, \frac{1}{2\rho\gamma_f c_f^2}\right) \tag{A8}$$

$$\eta^{(6)} = \left(0, \frac{1}{2\gamma_s c_s}, -\frac{b_y}{2b_x\alpha_s\gamma_s c_s}, -\frac{b_z}{2b_x\alpha_s\gamma_s c_s}, \frac{b_y}{2b_x^2\alpha_s\gamma_s}, \frac{b_z}{2b_x^2\alpha_s\gamma_s}, \frac{1}{2\rho\gamma_s c_s^2}\right) \tag{A9}$$

$$\eta^{(7)} = \left(0, -\frac{1}{2\gamma_s c_s}, \frac{b_y}{2b_x\alpha_s\gamma_s c_s}, \frac{b_z}{2b_x\alpha_s\gamma_s c_s}, \frac{b_y}{2b_x^2\alpha_s\gamma_s}, \frac{b_z}{2b_x^2\alpha_s\gamma_s}, \frac{1}{2\rho\gamma_s c_s^2}\right), \tag{A10}$$

while the right eigenvectors are:

$$\xi^{(1)} = (\rho, 0, 0, 0, 0, 0, 0) \tag{A11}$$

$$\xi^{(2)} = \left(0, 0, -\sigma\frac{b_z}{\sqrt{\rho}}, \sigma\frac{b_y}{\sqrt{\rho}}, b_z, -b_y, 0\right) \tag{A12}$$

$$\xi^{(3)} = \left(0, 0, \sigma\frac{b_z}{\sqrt{\rho}}, -\sigma\frac{b_y}{\sqrt{\rho}}, b_z, -b_y, 0\right) \tag{A13}$$

$$\xi^{(4)} = \left(\rho\frac{c_{ax}^2}{c_f^2}\alpha_f, c_f\frac{c_{ax}^2}{c_f^2}\alpha_f, -\frac{b_x b_y}{\rho c_f}, -\frac{b_x b_z}{\rho c_f}, b_y, b_z, \frac{c_{ax}^2}{c_f^2}\gamma p\alpha_f\right) \tag{A14}$$

$$\xi^{(5)} = \left(\rho\frac{c_{ax}^2}{c_f^2}\alpha_f, -c_f\frac{c_{ax}^2}{c_f^2}\alpha_f, \frac{b_x b_y}{\rho c_f}, \frac{b_x b_z}{\rho c_f}, b_y, b_z, \frac{c_{ax}^2}{c_f^2}\gamma p\alpha_f\right) \tag{A15}$$

$$\xi^{(6)} = \left(\rho\frac{c_{ax}^2}{c_s^2}\alpha_s, c_s\frac{c_{ax}^2}{c_s^2}\alpha_s, -\frac{b_x b_y}{\rho c_s}, -\frac{b_x b_z}{\rho c_s}, b_y, b_z, \frac{c_{ax}^2}{c_s^2}\gamma p\alpha_s\right) \tag{A16}$$

$$\xi^{(7)} = \left(\rho\frac{c_{ax}^2}{c_s^2}\alpha_s, -c_s\frac{c_{ax}^2}{c_s^2}\alpha_s, \frac{b_x b_y}{\rho c_s}, \frac{b_x b_z}{\rho c_s}, b_y, b_z, \frac{c_{ax}^2}{c_s^2}\gamma p\alpha_s\right). \tag{A17}$$

The symbols used in the above expressions are defined as

$$b_\perp = \sqrt{b_y^2 + b_z^2}, \quad \alpha_f = \left(\frac{c_f^2}{c_{ax}^2} - 1\right), \quad \gamma_f = \left(1 - \frac{c_{ax}^2 a^2}{c_f^4}\right)$$

$$\sigma = \frac{b_x}{|b_x|}, \quad \alpha_s = \left(\frac{c_s^2}{c_{ax}^2} - 1\right), \quad \gamma_s = \left(1 - \frac{c_{ax}^2 a^2}{c_s^4}\right).$$

The right eigenvectors (A11)–(A17) (as the left eigenvectors) are linearly independent, so they form a complete set of vectors in a seven dimensional space. This allows us to write the second term in the MHD Equation (A1) as a linear combination of the $\xi_i^{(k)}$:

$$A_{ij}\frac{\partial U_j}{\partial x} = \sum_k L^{(k)}\xi_i^{(k)}. \tag{A18}$$

The left-hand side of Equation (A18) contains the advective terms representing the propagation of perturbations in the x direction (i.e., across the boundary). In this equation the contribution of the different modes to the propagation is singled out as the coefficients $L^{(k)}$ representing the weight of each mode. Using expression (A18), we re-write the Equation (A1) in the form

$$\frac{\partial U_i}{\partial \tau} = -\sum_k L^{(k)}\xi_i^{(k)} - T_i, \tag{A19}$$

where the time derivatives of the fields U_i are expressed in terms of the coefficients $L^{(k)}$. Multiplying Equation (A19) by $\eta_i^{(k)}$ and using the condition (A3), we obtain the projected equation

$$L^{(k)} = -\eta_i^{(k)}\frac{\partial U_i}{\partial \tau} - \eta_i^{(k)}T_i, \tag{A20}$$

in which the coefficients $L^{(k)}$ are expressed as functions of the time derivatives $\partial U_i/\partial\tau$. Finally, another expression for $L^{(k)}$ is obtained by multiplying Equation (A18) by $\eta_i^{(k)}$:

$$L^{(k)} = \lambda^{(k)}\eta_i^{(k)}\frac{\partial U_i}{\partial x}, \tag{A21}$$

where we used Equation (A2) and the condition (A3). In Equation (A21) the coefficients $L^{(k)}$ are expressed in terms of the normal derivatives of the fields. Boundary conditions are determined using Equations (A19)–(A21) evaluated at the boundaries. In particular, Equation (A19) allows us to calculate the time evolution of the fields U_i at the boundaries once the coefficients $L^{(k)}$ have been determined.

Concerning the determination of $L^{(k)}$, we observe that boundary conditions can influence only incoming perturbations, whereas outgoing perturbations are entirely determined by the field configuration inside the domain. Therefore, the number of boundary conditions we can impose is equal to number of incoming modes. The first step of the procedure consists of calculating the sign of each eigenvalue $\lambda^{(k)}$ at the given gridpoint on the boundary, in order to distinguish between the $L^{(k)}$ corresponding to incoming perturbations and those corresponding to outgoing perturbations. Since the former coefficients are determined by boundary conditions, we must distinguish between the lower and the upper boundary.

A.1. Lower Boundary

On the lower boundary $x = 0$ we impose the value of the three components of the velocity field. In particular, we choose $v_x(x = 0, z, \tau) = 0$. In that case we have only three positive eigenvalues ($\lambda^{(2)}$, $\lambda^{(3)}$, and $\lambda^{(4)}$) corresponding to incoming Alfvén, fast and slow magnetosonic perturbations, three negative eigenvalues ($\lambda^{(5)}$, $\lambda^{(6)}$, and $\lambda^{(7)}$), while $\lambda^{(1)} = 0$. Since $\lambda^{(1)} = 0$, we can look at the entropy mode as an outgoing mode with null speed. The coefficients $L(1)$, $L^{(5)}$, $L^{(6)}$, and $L^{(7)}$ corresponding to outgoing perturbations are calculated using Equation (A21). The explicit expressions are the following:

$$L^{(1)} = 0 \tag{A22}$$

$$L^{(5)} = -\sigma\frac{b_x}{\sqrt{\rho}}\left[\sigma\frac{\sqrt{\rho}b_z}{2b_\perp^2}\left(\frac{\partial v_y}{\partial x}\right)_+ - \sigma\frac{\sqrt{\rho}b_y}{2b_\perp^2}\left(\frac{\partial v_z}{\partial x}\right)_+ + \frac{b_z}{2b_\perp^2}\left(\frac{\partial b_y}{\partial x}\right)_+ - \frac{b_y}{2b_\perp^2}\left(\frac{\partial b_z}{\partial x}\right)_+\right] \tag{A23}$$

$$L^{(6)} = -c_f\left[-\frac{1}{2\gamma_f c_f}\left(\frac{\partial v_x}{\partial x}\right)_+ + \frac{b_y}{2b_x\alpha_f\gamma_f c_f}\left(\frac{\partial v_y}{\partial x}\right)_+ + \frac{b_z}{2b_x\alpha_f\gamma_f c_f}\left(\frac{\partial v_z}{\partial x}\right)_+ \right.$$
$$\left. + \frac{b_y}{2b_x^2\alpha_f\gamma_f}\left(\frac{\partial b_y}{\partial x}\right)_+ + \frac{b_z}{2b_x^2\alpha_f\gamma_f}\left(\frac{\partial b_z}{\partial x}\right)_+ + \frac{1}{2\rho\gamma_f c_f^2}\left(\frac{\partial p}{\partial x}\right)_+\right] \tag{A24}$$

$$L^{(7)} = -c_s\left[-\frac{1}{2\gamma_s c_s}\left(\frac{\partial v_x}{\partial x}\right)_+ + \frac{b_y}{2b_x\alpha_s\gamma_s c_s}\left(\frac{\partial v_y}{\partial x}\right)_+ + \frac{b_z}{2b_x\alpha_s\gamma_s c_s}\left(\frac{\partial v_z}{\partial x}\right)_+ \right.$$
$$\left. + \frac{b_y}{2b_x^2\alpha_s\gamma_s}\left(\frac{\partial b_y}{\partial x}\right)_+ + \frac{b_z}{2b_x^2\alpha_s\gamma_s}\left(\frac{\partial b_z}{\partial x}\right)_+ + \frac{1}{2\rho\gamma_s c_s^2}\left(\frac{\partial p}{\partial x}\right)_+\right]. \tag{A25}$$

In these equations the lower symbol "+" indicates right x derivatives, which are calculated using boundary and internal gridpoints by a forward finite difference method. Thus, the internal configuration determines the coefficients $L^{(5)}$, $L^{(6)}$, and $L^{(7)}$ through these derivatives. The coefficients $L^{(2)}$, $L^{(3)}$, and $L^{(4)}$, corresponding to incoming perturbations, are determined by the velocity field imposed at the boundary by means of Equations (A19)–(A20), with $i = 2, 3, 4$, where $L^{(2)}$, $L^{(3)}$, and $L^{(4)}$ are treated as unknown. Solving these three equations, we find the explicit expressions for $L^{(2)}$, $L^{(3)}$, and $L^{(4)}$:

$$L^{(2)} = \frac{\sigma \sqrt{\rho} b_z}{b_\perp^2} \left(\frac{\partial v_y}{\partial \tau} + T_3 \right) - \frac{\sigma \sqrt{\rho} b_y}{b_\perp^2} \left(\frac{\partial v_z}{\partial \tau} + T_4 \right) + L^{(5)} \tag{A26}$$

$$L^{(3)} = -\frac{1}{\gamma_f c_f} T_2 + \frac{b_y}{b_x \alpha_f \gamma_f c_f} \left(\frac{\partial v_y}{\partial \tau} + T_3 \right) + \frac{b_z}{b_x \alpha_f \gamma_f c_f} \left(\frac{\partial v_z}{\partial \tau} + T_4 \right) + L^{(6)} \tag{A27}$$

$$L^{(4)} = -\frac{1}{\gamma_s c_s} T_2 + \frac{b_y}{b_x \alpha_s \gamma_s c_s} \left(\frac{\partial v_y}{\partial \tau} + T_3 \right) + \frac{b_z}{b_x \alpha_s \gamma_s c_s} \left(\frac{\partial v_z}{\partial \tau} + T_4 \right) + L^{(7)}. \tag{A28}$$

The quantities in the right-hand side of Equations (A26)–(A28) (velocity component time derivatives $\partial v_y / \partial \tau$, $\partial v_z / \partial \tau$; outgoing perturbation coefficients $L^{(5)}$, $L^{(6)}$, and $L^{(7)}$; and the quantities T_2, T_3, and T_4) are determined by the velocity field imposed at the boundary or by the configuration of fields in the interior of the domain. Thus, Equations (A26)–(A28) represent the compatibility conditions. Finally, the coefficients $L^{(k)}$ calculated by Equations (A22)–(A28) at a given time are used in Equation (A19) with $i = 1, 5, 6, 7$ to calculate the time advance of ρ, b_y, b_z, and p at the boundary $x = 0$.

A.2. Upper Boundary

The upper boundary $x = 1$ represents an open boundary that can be freely crossed by matter and/or outgoing perturbations. No velocity field is imposed on that boundary. Instead, boundary conditions correspond to the requirement that no incoming perturbations cross that boundary. In this case, since v_x can have any sign, the number of incoming or outgoing waves on a given gridpoint cannot be determined a priori. As for the lower boundary, coefficients $L^{(k)}$ corresponding to outgoing perturbations are determined by Equation (A21) that we write in the form

$$L_{\text{out}}^{(k)} = \lambda^{(k)} \eta_i^{(k)} \left(\frac{\partial U_i}{\partial x} \right)_- \ , \quad \text{for } (k) \text{ such that } \lambda^{(k)} \geqslant 0. \tag{A29}$$

The lower symbol "−" indicates left x-derivatives, which are calculated using boundary and internal gridpoints by a backward finite difference method. Coefficients $L^{(k)}$ corresponding to incoming perturbations are calculated using the projected MHD Equation (A20). In this equation we set

$$\eta_i^{(k)} \frac{\partial U_i}{\partial \tau} = 0, \quad \text{for } (k) \text{ such that } \lambda^{(k)} < 0, \tag{A30}$$

where only values of the index (k) corresponding to a negative eigenvalue $\lambda^{(k)}$ are considered. Equation (A30) represents the boundary conditions and corresponds to the requirement that incoming perturbations alone do not generate any time evolution of the fields U_i. Note that the number of boundary conditions (A30) is equal to the number of incoming perturbations at the given gridpoint. Using Equation (A30) into Equation (A20) we get the expression for the coefficients $L^{(k)}$ corresponding to incoming perturbations:

$$L_{\text{in}}^{(k)} = -\eta_i^{(k)} T_i, \quad \text{for } (k) \text{ such that } \lambda^{(k)} < 0. \tag{A31}$$

Finally, by inserting the coefficients $L^{(k)}$ (Equations (A29) and (A31)) into the Equation (A19), the time advance of all the fields U_i at the boundary $x = 1$ is calculated.

As claimed by Poinsot & Lele (1993), who applied this method for a fluid case in order to guarantee stability and/or well-posedness, it is necessary to add further boundary conditions. In our case, we impose that some diffusive terms in Equations (28)–(31) ($\kappa [\partial^2 (p/\rho)/\partial x^2]$, $\eta \nabla^2 b_y$, $\eta \nabla^2 b_z$) are vanishing at $x = 0$ and $x = 1$.

APPENDIX B

ANALYTICAL EXPRESSION OF THE VECTOR POTENTIAL

The magnetic field of our model can be expressed in terms of a vector potential $\mathbf{A}(x, z) = A(x, z)\mathbf{e}_y$:

$$\mathbf{b}(x, z) = \nabla \times (A(x, z)\mathbf{e}_y), \tag{B1}$$

where the following equations hold for the magnetic field components:

$$b_x(x, z) = -\frac{\partial A(x, z)}{\partial z} \tag{B2}$$

$$b_z(x, z) = \frac{\partial A(x, z)}{\partial x}. \tag{B3}$$

We derive an analytical expression for $A(x, z)$ as a function of the magnetic field components using the periodicity of b_x and b_z along the z direction. The magnetic field components can be written as

$$b_x(x, z) = \sum_{k_z} \hat{b}_x(x, k_z) e^{ik_z z} \tag{B4}$$

$$b_z(x, z) = \sum_{k_z} \hat{b}_z(x, k_z) e^{ik_z z}. \tag{B5}$$

Equations (B2)–(B5) establish that the partial derivatives of $A(x, z)$ have to be periodical functions of the variable z. The most general form of $A(x,z)$ that fulfills this condition is

$$A(x, z) = \sum_{k_z} \hat{A}(x, k_z) e^{ik_z z} + cz + A_0, \tag{B6}$$

where c and A_0 are both constants. The value of c and of the coefficients $\hat{A}(x, k_z)$ define A univocally. We can calculate them by substituting expression (B6) and Equations (B4) and (B5) in Equations (B2) and (B3):

$$\sum_{k_z} \hat{b}_x(x, k_z) e^{ik_z z} = -\sum_{k_z} ik_z \hat{A}(x, k_z) e^{ik_z z} - c \tag{B7}$$

$$\sum_{k_z} \hat{b}_z(x, k_z) e^{ik_z z} = \sum_{k_z} \frac{\partial \hat{A}(x, k_z)}{\partial x} e^{ik_z z}. \tag{B8}$$

From Equation (B7) we get

$$\hat{A}(x, k_z) = \frac{\hat{b}_x(x, k_z)}{-ik_z} \qquad \forall k_z \neq 0 \tag{B9}$$

$$c = -\hat{b}_x(x, 0), \tag{B10}$$

and from Equation (B8) we obtain the expression for $\hat{A}(x, 0)$:

$$\hat{A}(x, 0) = \int_0^x \hat{b}_z(x', 0) \, dx'. \tag{B11}$$

Using Equations (B9), (B10), and (B11) we have the analytical solution for $A(x,z)$:

$$A(x, z) = \int_0^x \hat{b}_z(x', 0) \, dx' + \sum_{k_z \neq 0} \frac{\hat{b}_x(x, k_z)}{-ik_z} e^{ik_z z} - \hat{b}_x(x, 0)z + A_0, \tag{B12}$$

where the constant A_0 is completely arbitrary. The vector potential $A(x,z)$ at any given time τ is numerically calculated using Equation (B12) where the Fourier coefficients $\hat{b}_x(x, 0)$ and $\hat{b}_z(x, k_z)$ are obtained by an FFT algorithm and the integral is computed with the Simpson's rule.

REFERENCES

Acton, L. W., Culhane, J. L., Wolfson, C. J., et al. 1981, ApJL, 224, L137
Banerjee, D., Gupta, G. R., & Teriaca, L. 2011, SSRv, 158, 267
Belcher, J. W., & Davis, L. 1971, JGR, 76, 3534
Buchlin, E., Cargill, P. J., Bradshaw, S. J., & Velli, M. 2007, A&A, 469, 347
Califano, F., Chiuderi, C., & Einaudi, G. 1990, ApJ, 365, 757
Califano, F., Chiuderi, C., & Einaudi, G. 1992, ApJ, 390, 560
Carbone, V., & Veltri, P. 1990, GApFD, 52, 153
Chae, J., Schühle, U., & Lemaire, P. 1998, ApJ, 505, 957
Cirtain, J. W., Golub, L., Lundquist, L., et al. 2007, Sci, 318, 1580
Cranmer, S. R., van Ballegooijen, A. A., & Edgar, R. J. 2007, ApJS, 171, 520
Davila, J. M. 1987, ApJ, 317, 514
DeForest, C. E., & Gurman, J. B. 1998, ApJL, 501, L217
DeForest, C. E., Hoeksema, J. T., Gurman, J. B., et al. 1997, SoPh, 175, 393
Grappin, R., Léorat, J., & Buttighoffer, A. 2000, A&A, 362, 342
Hellinger, P., Trávníček, P. M., Štěpán Štverák, , Matteini, L., & Velli, M. 2013, JGR, 118, 1351
Heyvaerts, J., & Priest, E. R. 1983, A&A, 117, 220
Hollweg, J. 1987, ApJ, 312, 880
Inglis, A. R., Nakariakov, V. M., & Melnikov, V. F. 2008, A&A, 487, 1147
Ito, H., Tsuneta, S., Shiota, D., Tokumaru, M., & Fujiki, K. 2010, ApJ, 719, 131
Kappraff, J. M., & Tataronis, J. A. 1977, JPlPh, 18, 209
Landi, S., Velli, M., & Einaudi, G. 2005, ApJ, 624, 392
Lee, E. M., & Roberts, B. 1986, ApJ, 301, 430
Malara, F. 2013, A&A, 549, A54
Malara, F., De Franceschis, M. F., & Veltri, P. 2003, A&A, 412, 529
Malara, F., De Franceschis, M. F., & Veltri, P. 2005, A&A, 443, 1033
Malara, F., Nigro, G., Veltri, P., & Onofri, M. 2012, SSRv, 172, 157
Malara, F., Petkaki, P., & Veltri, P. 2000, ApJ, 533, 523
Malara, F., Primavera, L., & Veltri, P. 1996, ApJ, 459, 347
Malara, F., Veltri, P., Chiuderi, C., & Einaudi, G. 1992, ApJ, 396, 297
Malara, F., Veltri, P., & De Franceschis, M. F. 2007, A&A, 467, 1275
Marino, R., Sorriso-Valvo, L., Carbone, V., et al. 2011, P&SS, 59, 592
Matthaeus, W. H. 1982, J. Geophys. Lett., 9, 660
Matthaeus, W. H., Zank, G. P., Oughton, S., Mullan, D. J., & Dmitruk, P. 1999, ApJL, 523, L93
Matthaeus, W. H., Zank, G. P., Smith, C. W., & Oughton, S. 1999, PhRvL, 82, 3444
McAteer, R. T. J., Gallagher, P. T., Brown, D. S., et al. 2005, ApJ, 620, 1101

McComas, D. J., Barraclough, B. L., Funsten, H. O., et al. 2000, JGR, 105, 10419
McIntosh, S. W., De Pontieu, B., Carlsson, M., et al. 2011, Natur, 475, 477
McLaughlin, J. A., De Moortel, I., Hood, A. W., & Brady, C. S. 2009, A&A, 493, 227
McLaughlin, J. A., Hood, A. W., & De Moortel, I. 2010, SSRv, 158, 205
Mitra-Kraev, U., Harra, L. K., Williams, D. R., & Kraev, E. 2005, A&A, 436, 1041
Mok, Y., & Einaudi, G. 1985, JPlPh, 33, 199
Murray, M. J., van Driel-Gesztelyi, L., & Baker, D. 2009, A&A, 494, 329
Nakagawa, Y., Hu, Y. Q., & Wu, S. T. 1987, A&A, 179, 354
Nakariakov, V. M., Roberts, B., & Murawski, K. 1997, SoPh, 175, 93
Nakariakov, V. M., Roberts, B., & Murawski, K. 1997, A&A, 332, 795
Nigro, G., Malara, F., Carbone, V., & Veltri, P. 2004, PhRvL, 92, 194501
Ofman, L., Nakarikov, V. M., & DeForest, C. E. 1999, ApJ, 514, 441
Ofman, L., Romoli, M., Poletto, G., Noci, G., & Kohl, J. L. 1997, ApJL, 491, L111
Onofri, M., Primavera, L., Malara, F., & Londrillo, P. 2007, JCoPh, 226, 1874
Petkaki, P., Malara, F., & Veltri, P. 1998, ApJ, 500, 483
Poinsot, T. J., & Lele, S. K. 1993, JCoPh, 101, 104
Ruderman, M. S., Nakariakov, V. M., & Roberts, B. 1998, A&A, 338, 1118
Shebalin, J. V., Matthaeus, W. H., & Montgomery, D. 1983, JPlPh, 29, 525
Shibata, K., Nakamura, T., Matsumoto, T., et al. 2007, Sci, 318, 1591
Similon, P. L., & Sudan, R. N. 1989, ApJ, 336, 442
Sorriso-Valvo, L., Marino, R., Carbone, V., et al. 2007, PhRvL, 99, 115001
Steinolfson, R. S. 1985, ApJ, 295, 213
Sun, M. T., Wu, S. T., & Dryer, M. 1995, JCoPh, 116, 330
Suzuki, T. K., & Inutsuka, S.-I. 2005, ApJL, 632, L49
Tomczyk, S., & McIntosh, S. W. 2009, ApJ, 697, 1384
Tomczyk, S., McIntosh, S. W., Keil, S. L., et al. 2007, Sci, 317, 1192
Van Doorsselaere, T., Nakariakov, V. M., & Verwichte, E. 2008, ApJL, 676, L73
Verdini, A., & Velli, M. 2007, ApJ, 662, 669
Verdini, A., Velli, M., & Buchlin, E. 2009, APJL, 700, L39
Verdini, A., Velli, M., Matthaeus, W. H., Oughton, S., & Dmitruk, P. 2010, ApJL, 708, L116
Wang, Y.-M., Grappin, R., Robbrecht, E., & Sheeley, N. R., Jr. 2012, ApJ, 749, 182
Wang, Y.-M., Sheeley, N. R., Jr., & Rich, N. B. 2007, ApJ, 658, 1340
Warren, H. P., Mariska, J. T., Wilhelm, K., & Lamaire, P. 1997, ApJL, 484, L91
Zhang, J., Ma, J., & Wang, H. 2006, ApJ, 649, 464